Hindawi
Structural Control and Health Monitoring
Volume 2023, Article ID 8897653, 27 pages
https://doi.org/10.1155/2023/8897653

Research Article

Three-Dimensional Prestressed Tuned Mass Damper for Passive Vibration Control of Coupled Multiple DOFs Offshore Wind Turbine

Zhenbo Lei,[1] **Gang Liu**,[1,2] **Xuesen Zhang**,[3] **Qingshan Yang**,[1,2] **and S. S. Law**[1,2]

[1]*School of Civil Engineering, Chongqing University, Chongqing 400045, China*
[2]*Key Laboratory of New Technology for Construction of Cities in Mountain Area, Chongqing University, Ministry of Education, Chongqing 400045, China*
[3]*CGN New Energy Holdings Co, Ltd., Beijing 100070, China*

Correspondence should be addressed to Gang Liu; gliu@cqu.edu.cn

Received 9 June 2023; Revised 5 August 2023; Accepted 28 August 2023; Published 14 September 2023

Academic Editor: Sara Casciati

Large megawatts offshore wind turbine (OWT) with low natural frequency and low damping is subjected to significant vibration from wind and wave actions in its service environment. The one-dimensional prestressed tuned mass damper (PSTMD) is further extended to a 3D-PSTMD for the control of vibrations of the OWT in this paper. A multiple DOFs coupled system of turbine, blades, tower, and foundation under aerodynamic and hydrodynamic forces is considered in this study of vibration mitigation at fore-aft and side-side directions. The dynamic model is derived with the Lagrangian equation, and the superiorities of the PSTMD are proved from the perspective of theoretical analysis. Aerodynamic and hydrodynamic loads are generated with the blade element momentum (BEM) theory and Morrison equation, and the dynamic responses of different systems are computed by using the Wilson-θ method. The analysis results indicate that a damping coefficient of the 3D-PSTMD corresponding to the first vibration mode can be tuned to take up values larger than that in traditional three-dimensional pendulum (TMD) (3D-PTMD). The bidirectional vibration suppression competences of the 3D-PSTMD in the dynamic responses when under aerodynamic and hydrodynamic loads are better than those of the traditional 3D-PTMD.

1. Introduction

The offshore wind turbine (OWT) has become more popular in recent years due to advantages of being a cheap energy source, less visual impact, low noisy problem, and without land requirement [1]. Taller and slender large-megawatts OWTs have been constructed offshore [2] to capture more energy. However, the steel OWT structure has a long vibration period and light damping which make it more vulnerable to significant vibrations caused by wind or waves [3]. These vibrations will further lead to adverse impacts on the efficiency of energy generation and the fatigue life [4] of the tower. Consequently, it is necessary to mitigate the structural vibrations to enable continuous operation of the turbine in the harsh offshore environments.

There are three types of vibration control methods for tall buildings and large span bridges, and they can be separated into three categories, such as active, semiactive, and passive vibration absorption technologies [5]. Passive vibration absorbers have been applied widely for vibration control of OWT because of its low cost and high stability [6]. Amongst these devices, tuned mass damper (TMD) has a wide range of application due to its simple configuration [7]. Two methods are usually employed to analyze the TMD-controlled OWT system. The OWT is simplified as a single degree-of-freedom (DOF) system for modelling the vibration behavior of the controlled OWT [8]. This has the advantage of obtaining the analytical design parameters of the TMD from the harmonic balance method (HBM) or frequency response function (FRF) [9]. Verma et al. [10]

utilized an efficient framework to optimally design the TMD control system. The optimal designed TMD was found effective for all cases of wind and wave loading studies. A multiple DOFs OWT system was also applied to numerically analyze the vibration energy dissipation capability of the TMD [11]. This multiple DOFs OWT system can be employed to model the vital aerodynamic and hydrodynamic forces on an actual engineering structure [12]. Sun and Jahangiri [13] utilized a three-dimensional pendulum TMD to mitigate the dynamic responses of the tower top. Results showed that the vibrations at the tower top under aerodynamic load induced by wind in both the fore-aft (F-A) and side-side (S-S) directions are reduced.

The abovementioned literature review also shows that the efficiency of the pendulum TMD decreases as the mass ratio decreases due to the limitation of available space inside the wind turbine tower [14]. The traditional pendulum TMD also has the disadvantage that the frequency of the damper can only be tuned by changing the pendulum length if the mass ratio is fixed [15]. Several new TMDs have been proposed in recent years to remove this limitation. For instance, Chapain and Aly [16] presented a pendulum pounding the TMD with viscoelastic boundary for vibration suppression in wind turbines. Results indicated that this pendulum pounding TMD has the remarkable energy absorption competence over the conventional TMD since its robustness. Jahangiri et al. [12] proposed a three-dimensional pounding pendulum TMD, which comprises of a pendulum mass damper along with a cylindrical pounding layer. Results showed that this device is more robust than the traditional pendulum TMD for vibration control of OWT. Subsequently, a novel prestressed tuned mass damper (PSTMD) was proposed by the authors with an additional cable beneath the mass for applying prestressing force in the cable of the traditional pendulum TMD [17]. The frequency of the PSTMD can then be tuned synchronously by changing the pendulum length and the tensile force of the prestressing cable. Numerical simulations indicated that vibration energy dissipation capability and the tuning effect of the PSTMD are greater than the corresponding conventional TMD when under harmonic load.

It should be noted that the PSTMD was considered as a single DOF system for obtaining its analytical design parameters on the basis of the virtual work principle [17], and only harmonic vibration in one direction is studied in the previous paper. However, the dynamic characteristics of an OWT at the F-A and S-S directions are clearly different, and the single DOF model of the wind turbine cannot prove the superiority of the PSTMD from the perspective of a theoretical analysis. Moreover, the blade, tower, and foundation should be taken as different DOFs because the aerodynamic force on the blade caused by wind and hydrodynamic force of foundation caused by wave action need to be considered separately to simulate better the actual environmental excitation. This paper developed a three-dimensional PS-TMD (3D-PSTMD) for vibration control of the OWT with the dynamic system modelled as coupling multiple DOFs of the blade, tower, and foundation and established the multiple source load model to simulate aerodynamic and hydrodynamic forces. More importantly, the superiorities of the PSTMD are proved from the perspective of a theoretical analysis in this paper when comparing with the traditional PTMD (see Section 3.5).

The paper is organized as follows. The dynamic model of OWT with the 3D-PSTMD is described in Section 2, and the equation of motion of the multiple DOFs OWT system with the 3D-PSTMD is derived in Section 3. The aerodynamic and hydrodynamic forces are derived in Section 4 using the BEM theory and Morrison equation. Numerical simulation of a 5 MW OWT is studied with the simulated wind-wave loads and the 3D-PTMD and 3D-PSTMD as designed in Section 5. The dynamic responses are computed by using the Wilson-θ method, and the energy dissipation competence of the 3D-PSTMD as compared to those from the traditional 3D-PTMD is assessed in Section 6. The corresponding conclusions are presented in Section 7.

2. Dynamic Model of OWT Coupled by 3D-PSTMD

2.1. OWT with 3D-PSTMD. The OWT coupled by a 3D-PSTMD structure under the wind-wave excitations is shown in Figure 1. The displayed OWT consists of three blades, nacelle, tower, and foundation. The 3D-PSTMD composed of three assemblies, i.e., a mass block for generating the opposite control force, the prestressed cables for tuning own frequency via tensile force and the suspension height, and three viscosity dampers for absorbing the corresponding oscillation energy from the OWT vibration. Since the OWT tower is a typical high and thin-wall structure and its structural model damping ratio is generally less than 1%, this structure is usually viewed as the classical lower damping system. Hence, the dynamic vibration absorber (DVA) is always used to promote the structural model damping and reduce the dynamic responses.

In this respect, the 3D-PSTMD may be considered as an improved DVA and oscillation dissipater on the basis of the conventional PTMD. As illustrated in Figure 1, the mass block is vertically assembled in position using the tensile force cables, and bottom cable is connected to the flange near the tower top. Within the horizontal plane, this mass block is linked to the tower tube wall via arranged viscosity dampers, as shown in Figure 1.

2.2. Mathematical Model. To simulate the corresponding aerodynamic and hydrodynamic forces, the blade rotation and soil interaction effects need to be considered. A fully coupled three-dimensional OWT is modelled as a 12 DOFs system, including 6 DOFs for the three turbine blades in the edgewise and flapwise directions, 2 DOFs for the tower at F-A and S-S directions, and 4 DOFs for the translation and rotation of foundation at F-A and S-S directions. The 3D-PSTMD is modelled with 2 DOFs in the fore-aft and side-side directions. The 14 DOFs for all components are denoted by symbols q_1~q_{14}, respectively, and they are listed in Table 1.

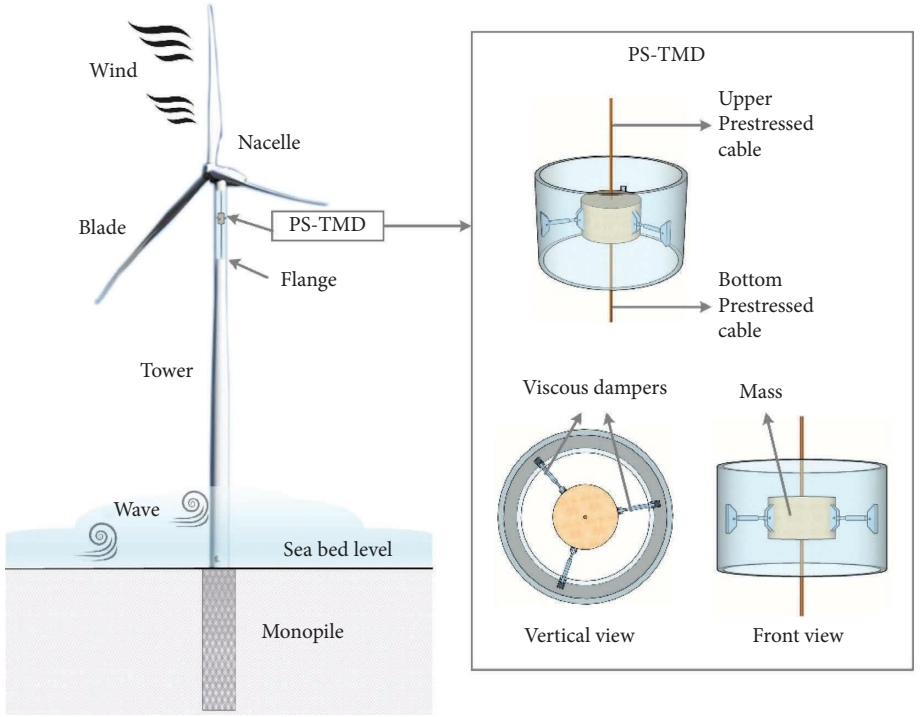

Figure 1: Conception design of OWT controlled by 3D-PSTMD.

Table 1: DOFs for different components of OWT with 3D-PSTMD.

Component		Flapwise or fore-aft direction	Edgewise or side-side direction
Blade	1	q_4	q_1
	2	q_5	q_2
	3	q_6	q_3
Tower		q_7	q_8
Foundation	Translation	q_9	q_{11}
	Rotation	q_{10}	q_{12}
3D-PSTMD		q_{13}	q_{14}

Note: The fore-aft direction of the tower or foundation is the same as the flapwise direction of the blade, and the side-side direction of the tower or foundation is the same as the edgewise direction of the blade.

Four coordinate systems (CSs), including a global CS ($Oxyz$) and three local CSs ($O_bx_by_bz_b$ for the blade, $O_tx_ty_tz_t$ for the tower, and $O_Px_Py_Pz_P$ for the 3D-PSTMD), as shown in Figures 2 and 3 are designed to express the absolute displacement of all assemblies. The DOFs q_1~q_3 denote the generalized displacements of three blade tips relative to the root of the blade in the edgewise direction. DOFs q_4~q_6 are similar displacements but in the flapwise direction. DOFs q_7 and q_8 denote the generalized displacements of the tower at F-A and S-S directions, respectively. The corresponding DOFs q_9 and q_{10} represent the translational and rotational displacements of monopile foundation in the F-A direction, and DOFs q_{11} and q_{12} are the translational and rotational displacements of monopile foundation in the S-S direction, respectively.

The $Q_{\text{wind}}(t)$ and $Q_{\text{wave}}(t)$ in Figure 2 denote the integral aerodynamic and hydrodynamic forces, respectively. Point O is the centroid of foundation, and x, y, and z are the F-A, S-S, and vertical coordinate axes of the OWT, respectively, with point O as origin. Point O_b is the centroid of the turbine hub of the OWT, and x_b, y_b, and z_b are the flapwise, edgewise, and vertical coordinates, respectively, with point O_b as origin. Point O_t denotes the centroid of the section at the toe of the tower, and x_t, y_t, and z_t are the F-A, S-S, and vertical coordinate axes, respectively, with point O_t as origin. Point O_P is the centroid of the 3D-PSTMD, and x_P, y_P, and z_P are the F-A, S-S and vertical coordinates for the 3D-PS-TMD, respectively. $\varphi_t(z_t)$ represents the shape function corresponding to the fundamental mode of the tower along z_t.

In Figure 3, dr is the infinitesimal unit of blade length, and r represents the distance from dr to the root of the blade. $\varphi_{be}(r)$ and $\varphi_{bf}(r)$ denote the shape function corresponding to the fundamental mode of the blade along r in the in-plane and out-plane, respectively. $u_b(r, t)$ is the generalized displacement of the infinitesimal unit length of the blade

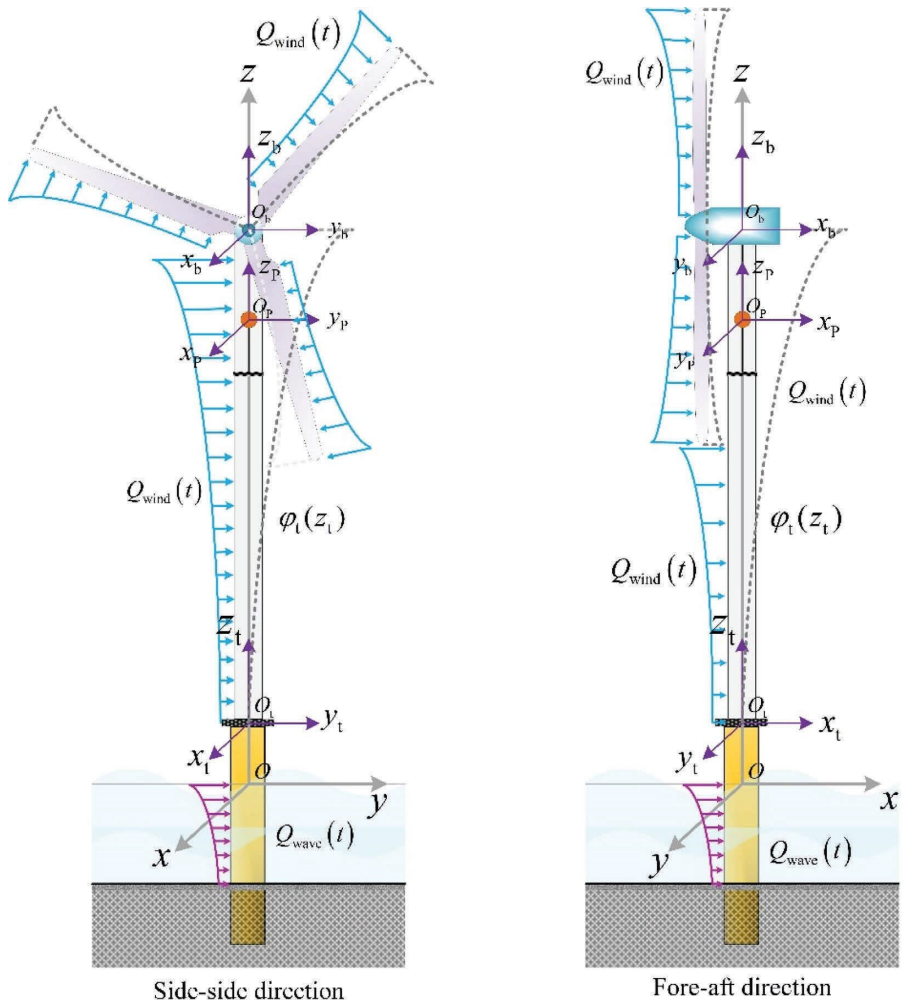

FIGURE 2: Global coordinate systems.

relative to the root of the blade, and θ_b represents the rotational angle of the blade. h_L represents the height suspending the 3D-PSTMD device, and h_F represents the uppermost segment height of the tower.

2.3. Generalized Absolute Displacement and Velocity. If the blade rotation velocity is assumed as ω_b, the azimuthal angle θ_b of the j^{th} blade can be expressed as shown in Figure 3 as

$$\theta_{bj} = \omega_b t + \frac{2\pi}{3}(j-1), \quad j = 1, 2, 3. \tag{1}$$

According to the local coordinate transformation relationship in Figure 3, the absolute displacements of the tower top (nacelle) at F-A and S-S directions in the *Oxyz* system can be obtained as

$$\begin{cases} x_{\text{nf}} = q_7 + q_9 + H\tan(q_{10}) \approx q_7 + q_9 + Hq_{10}, \\ x_{\text{ns}} = q_8 + q_{11} + H\tan(q_{12}) \approx q_8 + q_{11} + Hq_{12}, \end{cases} \tag{2}$$

where x_{nf} and x_{ns} are the generalized absolute displacement of nacelle at the F-A and S-S directions, respectively. Symbol H denotes the height of nacelle above the sea bed.

The generalized absolute velocities of nacelle in the *Oxyz* coordinate system at the F-A and S-S directions can be written as

$$\begin{cases} v_{\text{nf}} = \dot{q}_7 + \dot{q}_9 + H\dot{q}_{10}, \\ v_{\text{ns}} = \dot{q}_8 + \dot{q}_{11} + H\dot{q}_{12}, \end{cases} \tag{3}$$

where v_{nf} and v_{ns} are the absolute generalized velocities of nacelle in F-A and S-S directions, respectively.

As shown in Figure 3, the absolute generalized displacements of the infinitesimal unit dr of the blade in the *Oxyz* coordinate system can be obtained from equation (2) and the local coordinate transformation of the blade as

$$\begin{cases} x_{bej} = x_{\text{ns}} + r\sin\theta_{bj} + q_j\varphi_{bej}\cos\theta_{bj}, \\ x_{bfj} = x_{\text{nf}} + q_{j+3}\varphi_{bfj}, \\ x_{bzj} = r\cos\theta_{bj} - q_j\varphi_{bej}\sin\theta_{\text{b}j}, \end{cases} \tag{4}$$

where x_{bej}, x_{bfj}, and x_{bzj} represent the absolute displacements of the j^{th} blade along the edgewise (in-plane), flapwise (out-plane), and vertical directions, respectively. φ_{bej} and φ_{bfj} represent the shape function corresponding to the

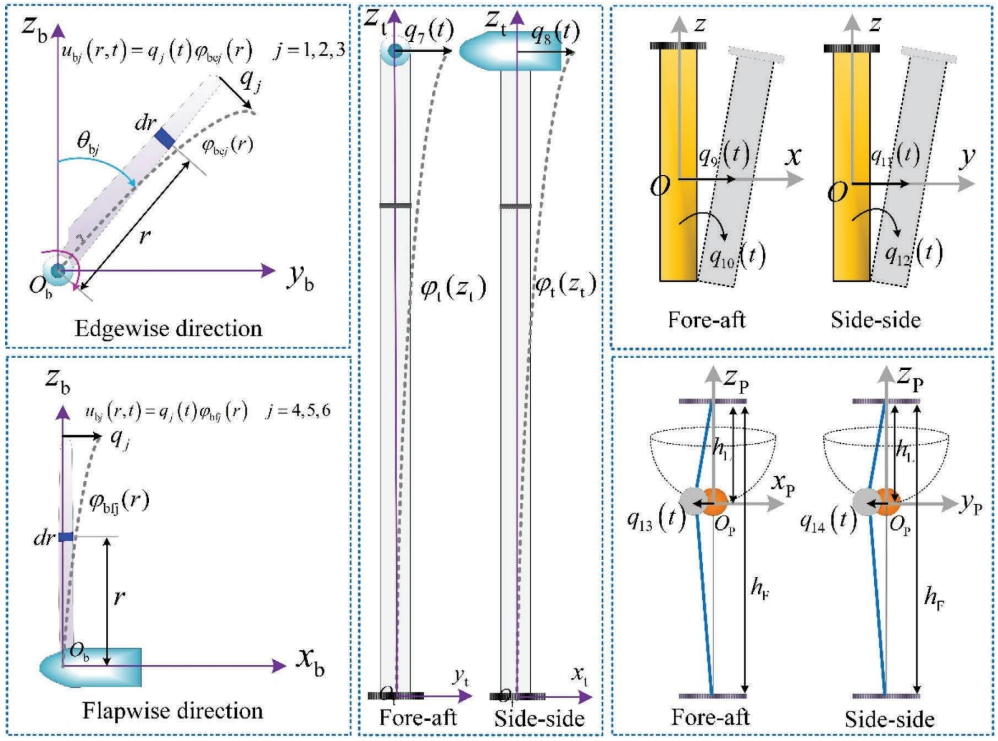

Figure 3: Local coordinate systems.

fundamental mode of the j^{th} blade in the in-plane and out-plane, respectively.

Taking the first derivative of equation (4), the absolute generalized velocity components of the infinitesimal unit dr of the j^{th} blade in the $Oxyz$ coordinate system are given as

$$\begin{cases} v_{bej} = v_{\text{ns}} + \omega_b r\cos\theta_{bj} + \dot{q}_j\varphi_{bej}\cos\theta_{bj} - \omega_b q_j\varphi_{bej}\sin\theta_{bj}, \\ v_{bfj} = v_{\text{nf}} + \dot{q}_{j+3}\varphi_{bfj}, \\ v_{bzj} = -\omega_b r\sin\theta_{bj} - \dot{q}_j\varphi_{bej}\sin\theta_{bj} - \omega_b q_j\varphi_{bej}\cos\theta_{bj}, \end{cases} \tag{5}$$

where v_{bej}, v_{bfj}, and v_{bzj} are the absolute generalized velocity components along the edgewise (in-plane), flapwise (out-plane), and vertical directions, respectively.

Since the position of the mass block of the 3D-PSTMD is connected in the vertical direction as shown in Figure 3, the vertical motion is minimal and can be ignored. Consequently, the absolute generalized displacements of the 3D-PSTMD are formulated as

$$\begin{cases} x_{Pf} = x_{nf} - q_{13}, \\ x_{Ps} = x_{ns} - q_{14}, \\ x_{Pz} = 0, \end{cases} \tag{6}$$

where x_{Pf} and x_{Ps} are the absolute generalized displacements of the 3D-PSTMD along the F-A, S-S, and vertical directions, respectively.

Consequently, the absolute generalized velocity components of the 3D-PSTMD along the F-A, S-S, and vertical directions can be, respectively, described as

$$\begin{cases} v_{Pf} = v_{nf} - \dot{q}_{13}, \\ v_{Pf} = v_{ns} - \dot{q}_{14}, \\ v_{Pz} = 0, \end{cases} \tag{7}$$

where v_{Pf} and v_{Ps} are the absolute generalized velocity components.

3. Equation of Motion and Dynamic Analysis

3.1. Lagrange Equation. Both the dashpot and servo-control (pitch controller or generator torque controller) technologies belong to the structural vibration control techniques of OWT [5, 15]. To not affect the tuning performance and adapting competence of dashpot for original environment loads, the servo-control system is ignored to establish the motion equation in this paper [11–13]. The Lagrange equation based on the Hamilton principle [18] is employed

to derive the structural dynamic equation of the OWT with and without the 3D-PSTMD device. The dynamic equation may be formulated as follows:

$$\frac{d}{\mathrm{d}t}\frac{\partial T\left[t,q_i(t),\dot{q}_i(t)\right]}{\partial \dot{q}_i(t)}-\frac{\partial T\left[t,q_i(t),\dot{q}_i(t)\right]}{\partial q_i(t)}+\frac{\partial V\left[t,q_i(t)\right]}{\partial q_i(t)}=Q_i(t), \tag{8}$$

where T represents the entire kinetic energy of the uncontrolled OWT system or controlled OWT system by the 3D-PSTMD. Symbol V denotes the entire potential energy for the uncontrolled OWT system or controlled OWT system by the 3D-PSTMD, and t is the time instant. $q_i(t)$ represents the generalized displacement vector of each DOF, and $\dot{q}_i(t)$ represents the generalized velocity vector. $Q_i(t)$ represents the generalized and nonconservative forces corresponding to i^{th} DOF vector. Symbol $\dot{(\,)}$ denotes the first derivative with regard to time.

3.2. Kinetic Energy. The resultant velocity of nacelle, v_n, in the *Oxyz* coordinate system can be obtained according to equation (3) as

$$v_n=\sqrt{v_{\mathrm{nf}}^2+v_{\mathrm{ns}}^2}. \tag{9}$$

The resultant velocity v_{bj} in the *Oxyz* coordinate system is obtained according to equation (5) as

$$v_{bj}=\sqrt{v_{bej}^2+v_{bfj}^2+v_{bzj}^2}. \tag{10}$$

Owing to the structural motions of OWT are teeny and neglected at the vertical direction, the resultant velocity v_t of an microunit dz of the tower in the *Oxyz* coordinate system can be expressed as

$$v_t=\sqrt{\left(\dot{q}_8\varphi_{\mathrm{t}}+\dot{q}_{11}+z\dot{q}_{12}\right)^2+\left(\dot{q}_7\varphi_{\mathrm{t}}+\dot{q}_9+z\dot{q}_{10}\right)^2}. \tag{11}$$

At the same time, the resultant velocity v_P of the 3D-PSTMD in the *Oxyz* coordinate system can be expressed according to equation (7) as

$$v_P=\sqrt{v_{\mathrm{Pf}}^2+v_{\mathrm{Ps}}^2}. \tag{12}$$

Therefore, the entire kinetic energy of OWT coupled by the 3D-PSTMD system is formulated as

$$T=\frac{1}{2}\sum_{j=1}^{3}\int_0^R m_b(r)v_{bj}^2(r,t)\mathrm{d}r+\frac{1}{2}M_n v_n^2+\frac{1}{2}\int_0^H M_{\mathrm{t}}(z)v_{\mathrm{t}}^2(z,t)\mathrm{d}z+\frac{1}{2}M_f\left[\dot{q}_9^2(t)+\dot{q}_{11}^2(t)\right]+\frac{1}{2}I_f\left[\dot{q}_{10}^2(t)+\dot{q}_{12}^2(t)\right]+\frac{1}{2}M_P v_P^2, \tag{13}$$

where R represents the blade length. $m_b(r)$ denotes the distributed mass along with radial blade length, and $M_t(z)$ is the distributed mass along the vertical height of the tower. M_P denotes the physical mass of the 3D-PSTMD. M_n represents the physical mass integrated by the nacelle and hub, and M_f represents the physical mass of monopile foundation. I_f represents the moment of inertia for monopile foundation.

3.3. Potential Energy. Considering the strain energy induced by the blade flexure, the centrifugal stiffening, and the gravity effect, the potential energy of the three turbine blades is computed. It can be expressed [13] as

$$V_b=\frac{1}{2}\sum_{j=1}^{3}\left[\left(k_{be}+k_{gee}-k_{gre}\cos\theta_{bj}\right)q_j^2+\left(k_{bf}+k_{gef}-k_{grf}\cos\theta_{bj}\right)q_{j+3}^2\right], \tag{14}$$

where V_b is the potential energy of the three blades. k_{be} and k_{bf} represent the lateral stiffness corresponding to the blade in the in-plane and out-plane, respectively. k_{gee} and k_{gef} represent the centrifugal stiffness in the in-plane and out-plane, respectively. k_{gre} and k_{grf} represent the blade stiffness induced by the gravity effect in the in-plane and out-plane, respectively. They are formulated as

$$\begin{cases} k_{be} = \int_0^R EI_{be}(r)\varphi_{be}''^2(r)\mathrm{d}r, \\ k_{bf} = \int_0^R EI_{bf}(r)\varphi_{bf}''^2(r)\mathrm{d}r, \\ k_{gee} = \omega_b^2 \int_0^R \int_r^R [m_b(r)r\mathrm{d}r]\varphi_{be}'^2(r)\mathrm{d}r, \\ k_{gef} = \omega_b^2 \int_0^R \int_r^R [m_b(r)r\mathrm{d}r]\varphi_{bf}'^2(r)\mathrm{d}r, \\ k_{gre} = \omega_b^2 \int_0^R \int_r^R [m_b(r)\mathrm{d}r]\varphi_{be}'^2(r)\mathrm{d}r, \\ k_{grf} = \omega_b^2 \int_0^R \int_r^R [m_b(r)\mathrm{d}r]\varphi_{bf}'^2(r)\mathrm{d}r, \end{cases} \tag{15}$$

where I_{be} and I_{bf} denote the inertial moments corresponding to the blade in the in-plane and out-plane, respectively, ω_b denotes the angular rotational velocity of blades, and g denotes the acceleration of gravity. Symbols $(\,)'$ and $(\,)''$ represent the first and second derivatives corresponding to radial length r of the blade.

Taking the static position of the 3D-PSTMD as reference, the corresponding potential energy V_P of the 3D-PSTMD device caused by cable tension is described as

$$V_P = \frac{1}{2}\left\{\frac{(M_P g + f_P)}{h_L}\left(q_{13}^2 + q_{14}^2\right) + \frac{f_P}{h_F - h_L}\left[(\varphi_{tP} - \varphi_{tF})q_7 - q_{13}\right]^2 + \frac{f_P}{h_F - h_L}\left[(\varphi_{tP} - \varphi_{tF})q_8 - q_{14}\right]^2\right\}, \tag{16}$$

where φ_{tP} and φ_{tF} denote the values of the tower shape function corresponding to the fundamental mode at the installation position of the 3D-PSTMD device and uppermost flange, respectively. h_L is the pendulum length of the 3D-PSTMD. f_P represents the tension of the prestressed cable.

Hence, the entire potential energy V of the OWT system controlled by the 3D-PSTMD device is formulated as

$$V = V_b + \frac{1}{2}k_t\left[q_7^2(t) + q_8^2(t)\right] + \frac{1}{2}k_{ft}\left[q_9^2(t) + q_{11}^2(t)\right] + \frac{1}{2}k_{fr}\left[q_{10}^2(t) + q_{12}^2(t)\right] + V_P, \tag{17}$$

where k_t denotes the lateral stiffness corresponding to the tower in the F-A and S-S directions. k_{ft} and k_{ft} represent the translational and rotational stiffness of monopile foundation at F-A and S-S directions, respectively.

3.4. Virtual Work Done by Damping Force. The damping force belongs to nonconservative force, and the corresponding virtual work done by these forces needs to be considered. When letting the static balance point of the 3D-PSTMD device as the reference position, the virtual work done by the damping force from the viscous damper in the 3D-PSTMD is obtained as

$$W_P = c_{Pf}\left(\varphi_{tP}\dot{q}_7 - \dot{q}_{13}\right)\left(\varphi_{tp}\delta q_7 - \delta q_{13}\right) + c_{Ps}\left(\varphi_{tP}\dot{q}_8 - \dot{q}_{14}\right)\left(\varphi_{tp}\delta q_8 - \delta q_{14}\right), \tag{18}$$

where W_P is the work done and c_{Pf} and c_{Ps} represent the integral damping coefficients from the three viscosity dampers in the 3D-PSTMD.

The total works done by the damping force in the OWT system coupled by the 3D-PSTMD device are gained as

$$\begin{aligned}\delta W = &\left[\dot{q}_j \alpha \sum_{j=1}^{3} \int_0^R EI_{be}(r)\varphi_{be}''(r)\mathrm{d}r\right]\delta q_j + \left[\dot{q}_{j+3}\alpha \sum_{j=1}^{3} \int_0^R EI_{bf}(r)\varphi_{bf}''(r)\mathrm{d}r\right]\delta q_{j+3} + \alpha\left(\dot{q}_7\delta q_7 + \dot{q}_8\delta q_8\right)\int_0^R EI_t(z)\varphi_t''(z)dz \\ &+ c_{ft}\left(\dot{q}_9\delta q_9 + \dot{q}_{11}\delta q_{11}\right) + c_{fr}\left(\dot{q}_{10}\delta q_{10} + \dot{q}_{12}\delta q_{12}\right) + c_{Pf}\left(\varphi_{tp}\dot{q}_7 - \dot{q}_{13}\right)\left(\varphi_{tp}\delta q_7 - \delta q_{13}\right) + c_{Ps}\left(\varphi_{tp}\dot{q}_8 - \dot{q}_{14}\right)\left(\varphi_{tp}\delta q_8 - \delta q_{14}\right),\end{aligned} \tag{19}$$

where c_{be} and c_{bf} are the damping coefficients of the tower in the edgewise and flapwise directions, respectively. I_t is the inertial moment corresponding to the tower in the F-A and S-S directions. α denotes the material damping constant. c_{ft} and c_{fr} are, respectively, the translational and rotational damping coefficients for monopile foundation in the F-A and S-S directions.

The equation of motion can be written in the matrix form by substituting equations (13), (17), and (19) into equation (8) as

$$\mathbf{M}\ddot{\mathbf{q}} + \mathbf{C}\dot{\mathbf{q}} + \mathbf{K}\mathbf{q} = \mathbf{Q}_{\text{wind}}(t) + \mathbf{Q}_{\text{wave}}(t), \tag{20}$$

where $\mathbf{Q}_{\text{wind}}(t)$ and $\mathbf{Q}_{\text{wave}}(t)$ represent the aerodynamic and hydrodynamic forces, respectively, which will be discussed later. $\ddot{\mathbf{q}}$, $\dot{\mathbf{q}}$, and $\mathbf{q}$ represent, respectively, the column vectors corresponding to dynamic responses of the uncontrolled OWT system or controlled system by the 3D-PSTMD.

$\mathbf{M}$ represents the mass matrix of the uncontrolled OWT structure or OWT coupled by the 3D-PSTMD device system, and $\mathbf{C}$ and $\mathbf{K}$ represent the corresponding damping and stiffness matrices, respectively. Their detailed expressions are shown in Appendixes A and B, respectively. An inspection shows that only the mass, stiffness, and damping matrices of the tower at F-A and S-S directions (DOFs q_7 and q_8) have changed after the inclusion of the 3D-PSTMD inside the tower. This is because that the local motion of the 3D-PSTMD is directly related to the motion of the nacelle and tower, as shown in equations (7) and (16).

3.5. Advantages of 3D-PSTMD. According to equations (A7), (A10), (B3), and (B6), the tower stiffness and damping coefficients of the OWT structure with and without the 3D-PSTMD device are written as

$$\begin{cases} k_{tU} = \displaystyle\int_0^H EI_t(z)\varphi''(z)^2\mathrm{d}z - M_n g\int_0^H \varphi'(z)^2\mathrm{d}z, \\ k_{tC} = \displaystyle\int_0^H EI_t(z)\varphi''(z)^2\mathrm{d}z - M_n g\int_0^H \varphi'(z)^2\mathrm{d}z + \frac{f_P\left(\varphi_{\text{tP}}^2 - \varphi_{\text{tF}}^2\right)}{h_F - h_L}, \end{cases} \tag{21}$$

$$\begin{cases} c_{tU} = \alpha\displaystyle\int_0^R EI_t(z)\varphi_t''(z)\mathrm{d}z, \\ c_{tC} = \alpha\displaystyle\int_0^R EI_t(z)\varphi_t''(z)\mathrm{d}z + \varphi_{tP}^2 c_{Pf}, \end{cases} \tag{22}$$

where subscript U and C denote, respectively, the uncontrolled OWT structure and OWT coupled by the 3D-PSTMD system. Symbols $(\,)'$ and $(\,)''$ represent the first and second derivatives with regard to tower height z.

A comparison of equation (21) shows that the 3D-PSTMD can provide an additional local stiffness to the OWT tower, and this means that the 3D-PSTMD can reduce the static displacement of the tower. It is worth to note that this is different from the traditional pendulum TMD because the 3D-PSTMD has an extra prestressed tensile force from the prestressed cables that acts directly within the topmost segment of the tower only. Its effect on reducing the static displacement is very small, as the prestressed tensile force is very small relative to elastic restoration force from the lateral stiffness of the tower.

Moreover, like the traditional pendulum TMD, the 3D-PSTMD can also provide additional damping to the OWT tower, as shown in equation (22). The mode damping coefficient of OWT coupled by the 3D-PSTMD system will be larger than that of the traditional pendulum TMD. This will greatly mitigate the excessive vibration of the OWT tower. More importantly, the 3D-PSTMD frequency is synchronously tuned by changing the cable tension and the suspension height, as shown in equation (B8). Figure 4 also

shows that the suspension height of the 3D-PSTMD is shorter than that of the traditional pendulum TMD. This illustrates that the 3D-PSTMD is closer to the tower top relative to the traditional pendulum TMD, and this leads to a large shape function value φ_t for the 3D-PSTMD. The abovementioned features of the OWT structure coupled by the 3D-PSTMD device are responsible for the better vibration mitigation effects compared to an OWT with the traditional pendulum TMD.

4. Aerodynamic and Hydrodynamic Loads

4.1. Aerodynamic Load

4.1.1. Wind Velocity Simulation. The wind velocity $v(z)$ consists of a constant mean velocity $\overline{v}(z)$ and a turbulent component $\widetilde{v}(z)$, and it is expressed as

$$v(z) = \overline{v}(z) + \widetilde{v}(z). \tag{23}$$

In this study, the exponential wind profile is adopted to calculate the mean velocity as

$$v(z) = v_r\left(\frac{z}{z_r}\right)^{\alpha_{\text{win}}}, \tag{24}$$

where z_r is the reference height, and v_r is the mean velocity at the reference height. α_{win} is the exponent of the wind profile.

The turbulent wind velocity is calculated by using the Davenport spectral model [19], which can be described as

$$S_v(z,n) = \overline{v}_{10}^2\frac{x^2}{n\left(1+x^2\right)^{4/3}}, \tag{25}$$

where n denotes the frequency of turbulent wind in Hz. x represents an intermediate coefficient, which is described as

$$x = \frac{1200n}{\overline{v}_{10}^2}, \tag{26}$$

where $\overline{v}_{10}$ represents the average wind speed at the reference altitude 10 m.

To account for the spatial dependency S_c of wind velocity at different points, the cross spectra between two points p_1 and p_2 are defined as

$$S_c(r,n) = \sqrt{S(p_1,n)\cdot S(p_2,n)}\cdot \text{Coh}(r,n), \tag{27}$$

where r is the distance between p_1 and p_2, and Coh (r, n) is the coherence function.

According to the Davenport spectral mode, the spatial coherence function [20] is expressed as

$$\text{Coh}(r,n) = e^{-\left[2n\cdot C_z\left(z_1-z_2\right)/v\left(z_1\right)+v\left(z_2\right)\right]}, \tag{28}$$

where z_1 and z_2 are the height at the reference points p_1 and p_2, respectively. C_z is the attenuation coefficient of the spectral mode, and it is usually taken as 10.

The turbulent wind velocity can be obtained from equations (25), (27), and (28), as

$$v(t) = \sum_{l=n}^{N}\left|H\left(\omega_{\text{win}}\right)\right|\cdot\sqrt{2\Delta\omega_{\text{win}}}\cdot\cos\left[\omega_{\text{win}}t+\theta_{\text{win}}\right], \tag{29}$$

where H (ω_{win}) is the matrix norm, and ω_{win} denotes the frequency of fluctuating wind in rad/s. θ_{win} represents the random phase angle, which is averagely distributed from 0 to 2π.

4.1.2. Generalized Aerodynamic Force. According to the BEM method [21], an integral blade section may be dispersed into N elements as shown in Figure 5(a), where R is the radial length of the rotor and ω_b is the angular rotation speed of the blade. The BEM method assumes that no radial dependency exists along the blade span, and thus, the blade elements can be analyzed independently with the momentum theory.

In Figure 5(a), dr is an increment along the span length and c (r) is the chord length at the mid-depth section of the blade. An arbitrary blade element having local velocities and aerodynamic load is shown in Figure 5(b). The relative wind velocity v_{rel} corresponding to the blade element dr in Figure 5(b) is described as

$$v_{\text{rel}} = \sqrt{\left[v(1-a)\right]^2+\left[\omega_b r\left(1+a'\right)\right]^2}, \tag{30}$$

where a and a' represent the induction factors corresponding to the axial and tangential velocities, which are obtained via iterations [22].

The flow angle ϕ can also be calculated on the basis of the BEM theory as

$$\phi = \arctan\left[\frac{v(1-a)}{\omega_b r\left(1+a'\right)}\right]. \tag{31}$$

According to Figure 5, the wind attack angle between relative wind velocity and chord line in Figure 5(b) can be expressed as

$$\alpha_b = \phi - \theta, \tag{32}$$

where θ represents the integrated angle between the pitch and twist angles, which is obtained from the airfoil data of the blade.

The lift and drag coefficients C_L and C_D can be obtained with the wind attack angle in equation (32) from airfoil data of the blade. Meanwhile, the lift force p_L perpendicular to and the drag force p_D parallel to the relative velocity can be computed as

$$\begin{cases} p_L = \dfrac{1}{2}\rho v_{\text{rel}}^2 c C_L, \\ \\ p_D = \dfrac{1}{2}\rho v_{\text{rel}}^2 c C_D, \end{cases} \tag{33}$$

where ρ represents the density of the blade, and c is the corresponding chord length.

The normal and the tangential coefficients C_N and C_T are defined as

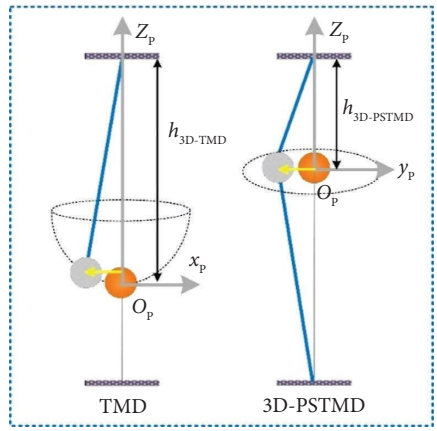

FIGURE 4: Comparison between 3D-PSTMD and traditional pendulum TMD.

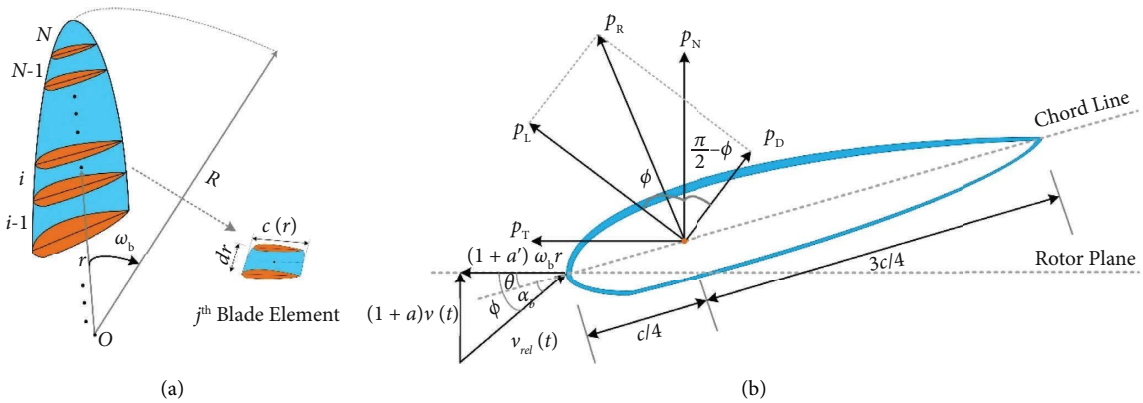

FIGURE 5: Schematic model of blade dispersed into (N) blade elements: (a) blade elements for BEM analysis and (b) blade element section.

$$\begin{cases} C_N = C_L \cos\phi + C_D \sin\phi, \\ C_T = C_L \sin\phi - C_D \cos\phi. \end{cases} \tag{34}$$

Hence, the normal and tangential forces p_N and p_T can be calculated as

$$\begin{cases} p_N = \dfrac{1}{2}\rho v_{\text{rel}}^2 c C_N, \\ p_T = \dfrac{1}{2}\rho v_{\text{rel}}^2 c C_T. \end{cases} \tag{35}$$

Combining Figures 3 and 5(b) with equation (35) on the basis of the virtual work principle, the virtual work done δW_{wind} by the normal and tangential forces p_N and p_T is obtained as

$$\delta W_{\text{wind}} = \sum_{j=1}^{3} \left\{ \int_0^R p_{Tj}(r,t)\left[\varphi_{be j}\delta q_j + \delta x_{ns}\cos\theta_{bj}\right]\mathrm{d}r + \int_0^R p_{Nj}(r,t)\left[\varphi_{bf j}\delta q_{j+3} + \delta x_{nf}\right]\mathrm{d}r \right\}, \tag{36}$$

where p_{Tj} (r, t) and p_{Nj} (r, t) represent the tangential and normal distribution wind load on the j^{th} blade.

The generalized aerodynamic force $Q_{\text{wind}}(t)$ then is obtained on the basis of the principles of the virtual work [23], and it is expressed as

$$Q_{\text{wind}}(t) = \frac{\partial(\delta W_{\text{wind}})}{\partial(\delta q_k)}, \tag{37}$$

where k represents the DOFs corresponding to different components of the OWT structure.

After combining equation (36) with equation (37), the aerodynamic force caused by wind load can be obtained as

$$Q_{\text{wind},k} = \begin{cases} \int_0^R p_{Tj}(r,t)\varphi_{\text{be}j}(r)\mathrm{d}r, & k = 1,2,3 \;\; j = 1,2,3, \\ \int_0^R p_{Nj}(r,t)\varphi_{\text{bf}j}(r)\mathrm{d}r, & k = 4,5,6 \;\; j = 1,2,3, \\ \sum_{j=1}^{3}\int_0^R p_{Nj}(r,t)\varphi_{\text{bf}j}(r)\mathrm{d}r, & k = 7,9 \;\; j = 1,2,3, \\ \sum_{j=1}^{3}\int_0^R p_{Tj}(r,t)\varphi_{\text{be}j}(r)\mathrm{d}r\cos\theta_{\text{b}j}, & k = 8,11 \;\; j = 1,2,3, \\ H\sum_{j=1}^{3}\int_0^R p_{Nj}(r,t)\varphi_{\text{bf}j}(r)\mathrm{d}r, & k = 10 \;\; j = 1,2,3, \\ H\sum_{j=1}^{3}\int_0^R p_{Tj}(r,t)\varphi_{\text{be}j}(r)\mathrm{d}r\cos\theta_{\text{b}j}, & k = 12 \;\; j = 1,2,3, \end{cases} \tag{38}$$

where the symbol j represents the j^{th} blade.

4.2. Hydrodynamic Force. In this study, the Morrison equation [24] is adopted to calculate the hydrodynamic force on circular cylindrical monopile of the OWT induced by wave action, and it can be expressed as

$$Q_{\text{wave}}(t) = \int_0^d \frac{1}{2}C_D\rho d_e\dot{u}(t)|\dot{u}(t)|\mathrm{d}z + \frac{1}{4}C_M\rho\pi d_e^2\ddot{u}(t)\mathrm{d}z, \tag{39}$$

where ρ is the sea water density, and its value is usually taken as 1025 kg/m^3. d_e is the monopile diameter of the OWT tower. C_M and C_D are the mass and drag coefficients, and their values are taken as 1.0 and 1.2, respectively, in the present study [12, 13]. $\ddot{u}$ and $\dot{u}$ are, respectively, the horizontal acceleration and velocity of monopole induced by wave action.

To simulate the random wave time history, the Pierson–Moskowitz (P-M) spectrum [25] is adopted as

$$S(\omega) = \frac{\alpha_{\text{wa}}g^2}{\omega_{\text{wa}}^5}e^{\left[-\beta\left(g/\omega_{\text{wa}}U_{19.5}\right)^4\right]}, \tag{40}$$

where α_{wa} and β represent two constants of the P-M wave spectrum, and the corresponding parameter values are, respectively, taken as 0.0081 and 0.74 in this paper. ω_{wa} denotes the frequency of the random wave in rad/s, $U_{19.5}$ represents the average wind speed corresponding to the reference altitude 19.5 m.

Based on the P-M spectrum representation method, the wave elevation $\eta(t)$, the wave velocity $\dot{u}$, and the acceleration $\ddot{u}$ can be expressed as

$$\begin{cases} \eta(t) = \sum_{i=1}^{M} a_{\text{wa}i}\cos\left(\omega_{\text{wa}i}t + \varepsilon_i\right), \\ a_{\text{wa}i} = \sqrt{2S\left(\omega_{\text{wa}i}\right)\Delta\omega_{\text{wa}i}}, \\ \dot{u}(z,t) = \sum_{i=1}^{M} a_{\text{wa}i}\omega_{\text{wa}i}\dfrac{\cosh\left(k_i d_{\text{wa}}\right)}{\sinh\left(k_i d_{\text{wa}}\right)}\cos\left(\omega_{\text{wa}i}t + \varepsilon_i\right), \\ \ddot{u}(z,t) = -\sum_{i=1}^{M} a_{\text{wa}i}\omega_{\text{wa}i}^2\dfrac{\cosh\left(k_i d_{\text{wa}}\right)}{\sinh\left(k_i d_{\text{wa}}\right)}\sin\left(\omega_{\text{wa}i}t + \varepsilon_i\right), \end{cases} \tag{41}$$

where d_w is the water depth, and ε is a random phase angle uniformly distributed from 0 to 2π [12, 13]. κ is the wave number per meter distance, and parameters ω_{wa} and κ represent the dispersion equation when the water depth z is given as

$$\kappa \tan h\kappa z_{\mathrm{wa}} = \frac{\omega_{\mathrm{wa}}^2}{g}. \tag{42}$$

According to equation (39) and the virtual work principle, the virtual work δW_{wave} done by the hydrodynamic force corresponding to the virtual displacement δq is written as

$$\delta W_{\mathrm{wave}} = \int_{-d_w}^{\eta(t)} \mathrm{dQ}_{\mathrm{wave}} \left[\varphi_t \left(\delta q_7 + \delta q_8\right) + \left(\delta q_9 + \delta q_{11}\right) + z\left(\delta q_{10} + \delta q_{12}\right)\right]. \tag{43}$$

After combining equation (43) with equation (37), the generalized hydrodynamic forces caused by wave action can be obtained as

$$\begin{cases} Q_{\mathrm{wave7}}(t) = Q_{\mathrm{wave8}}(t) = \displaystyle\int_{-\mathrm{d}w}^{\eta(t)} \varphi_t(z)\mathrm{d}F = \sum_{i=1}^{N_z} \varphi_{\mathrm{t}}(z)\left[\frac{\rho\pi d_e^2(z_i)}{4} C_M \ddot{u}(z_i,t)\Delta z + \frac{\rho}{2} C_D d_e(z_i)\dot{u}(z_i,t)\left|\dot{u}(z_i,t)\right|\Delta z\right], \\ Q_{\mathrm{wave9}}(t) = Q_{\mathrm{wave11}}(t) = \displaystyle\int_{-\mathrm{d}w}^{\eta(t)} \mathrm{d}F = \sum_{i=1}^{N_z}\left[\frac{\rho\pi d_e^2(z_i)}{4} C_M \ddot{u}(z_i,t)\Delta z + \frac{\rho}{2} C_D d_e(z_i)\dot{u}(z_i,t)\left|\dot{u}(z_i,t)\right|\Delta z\right], \\ Q_{\mathrm{wave10}}(t) = Q_{\mathrm{wave12}}(t) = \displaystyle\int_{-\mathrm{d}w}^{\eta(t)} z\mathrm{d}F = \sum_{i=1}^{N_z} z_i\left[\frac{\rho\pi d_e^2(z_i)}{4} C_M \ddot{u}(z_i,t)\Delta z + \frac{\rho}{2} C_D d_e(z_i)\dot{u}(z_i,t)\left|\dot{u}(z_i,t)\right|\Delta z\right], \end{cases} \tag{44}$$

where N_z represents the number of discrete segments for monopile foundation, and the symbol $\triangle z$ represents the segment length in the tower wetted portion.

5. Numerical Simulation

5.1. OWT Properties. A 5 MW monopile OWT from the National Renewable Energy Laboratory (NREL) is adopted in the present study. The Young modulus of the material for the OWT structure is 2.06×10^5 MPa, and its Poisson ratio and density are 0.3 and 7850 kg/m^3, respectively. The mean diameter and thickness of the tower linearly changes from the tower base to the tower top, and the blades' length and weight are 61.5 m and 1.774×10^4 kg, respectively. The main physical and geometrical parameters of this 5 MW OWT are shown in Table 2, according to the study in [26, 27].

5.2. Load Design. According to the Davenport spectral model in Section 4.1.1 and the OWT parameters in Section 5.1, the aerodynamic force is simulated by the BEM method. The mean wind speed $\overline{v}(t)$ is taken as 12 m/s at the height of the turbine hub, and the phase angle of random wind averagely distributed from 0 to 2π. The wind velocity of the blade and wind design spectrum are plotted in Figures 6(a) and 6(b) from equations (23)–(29).

Figure 6(b) shows that the wind design spectrum agrees very well with the Davenport spectrum indicating that the simulated wind record is capable of representing the wind velocity in the wind field.

It is also noted that the wind speed acting on each discrete blade element will change with the blade angle of rotation. Thus, considering the blade rotation speed in equation (30), the aerodynamic load on blades and tower corresponding to the simulated wind speed can then be obtained from equations (30)–(38), as shown in Figure 7. The load amplitude induced by wind in the F-A direction and S-S direction is notably different. This may be because the distinguishing normal and tangential coefficients in equation (34) are used to generate the corresponding aerodynamic force.

The Morrison equation is employed to simulate the hydrodynamic force based on the P-M spectrum in Section 4.2, and the random phase angle of the wave is uniformly distributed from 0 to 2π [12, 13]. Then, the distribution of wave velocity and wave acceleration in time and space can be obtained according to equations (40) and (41) using the MATLAB software.

The wave height and hydrodynamic load on the foundation and tower corresponding to the simulated wave velocity and acceleration can then be obtained from equation (44), as shown in Figure 9.

Table 2: Main parameters of the NREL 5 MW OWT.

Item	Description	Value
Gross properties	Power	5 MW
	Hub vertical height	87.6 m
	Cut-in, rated, and cut-out wind speed	3 m/s, 11.4 m/s, and 25 m/s
	Cut-in and rated rotor speed	6.9 rpm and 12.1 rpm
Blade	Radial length	61.5 m
	Physical mass	1.774×10^4 kg
	First inertial moment of mass	3.632×10^5 kg.m
	Fundamental frequency (in-plane)	0.87 Hz
	Fundamental frequency (out-plane)	1.06 Hz
	Damping ratio (in-plane and out-plane)	0.48%
Nacelle + hub	Physical mass (nacelle)	2.40×10^5 kg
	Physical mass (hub)	5.68×10^4 kg
Tower	Physical mass (tower)	2.68×10^5 kg
	Fundamental frequency (F-A direction)	0.324 Hz
	Fundamental frequency (S-S direction)	0.312 Hz
	Mode damping ratio (F-A and S-S directions)	1.0%
Foundation	Monopile mean diameter	1.6 m
	Sea water depth	20 m

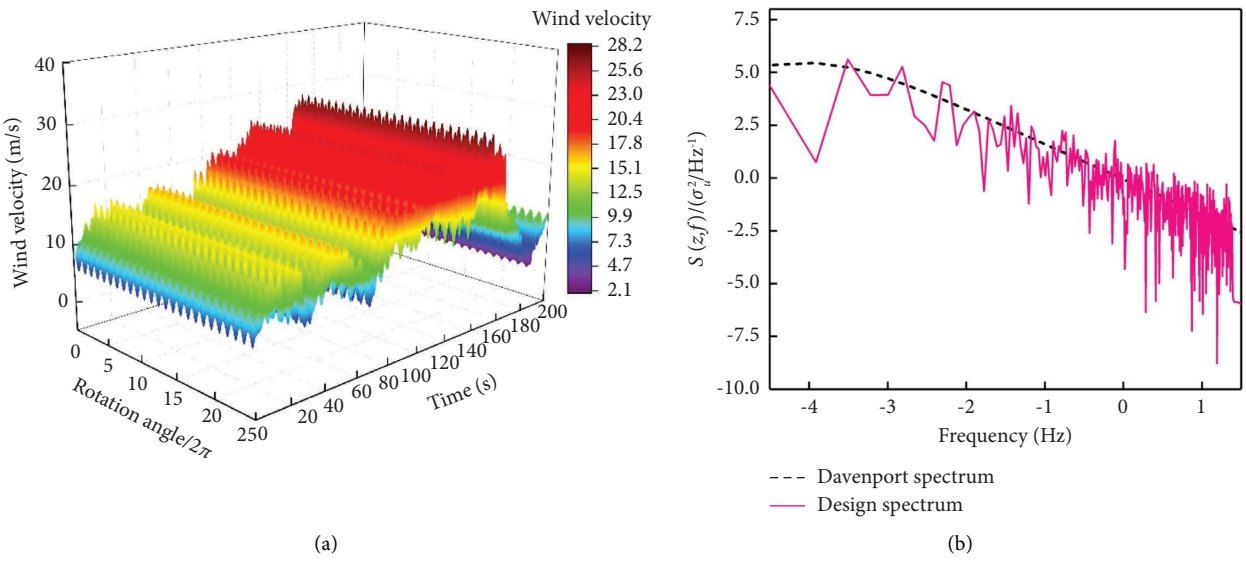

Figure 6: (a) Wind velocity and (b) wind design spectrum.

It is noted in Figures 8 and 9 that the acceleration, velocity, height, and hydrodynamic load of the wave action will change with the physical distance between the point considered and the monopile foundation. This is because of the notable influence of physical distance to the phase angle of stochastic wave loading when the harmonic-superposition theory is used in the computation. Subsequently, the wave number and hydrodynamic load of tower-changing trends are plotted in Figure 10. In contrast, the wave number depends more on the circular frequency of the random wave than the water depth; this point can be also seen in equation (42). In addition, unlike the aerodynamic load amplitude, the hydrodynamic load amplitude of the tower at F-A and S-S directions induced by wave has only a small difference since the properties of the circular monopile foundation are the same in both directions.

5.3. Dynamic Model Validation. To analyze the rationality of the developed dynamic model in Sections 3 and 4, a 5 MW OWT simulation model is established by using OpenFAST to calculate the fundamental frequencies and dynamic responses of the blade and tower and compared them with the calculation results of the developed model from MATLAB. The geometric and physical parameters of 5 MW OWT can be found in the studies in [28]; then, substituting these

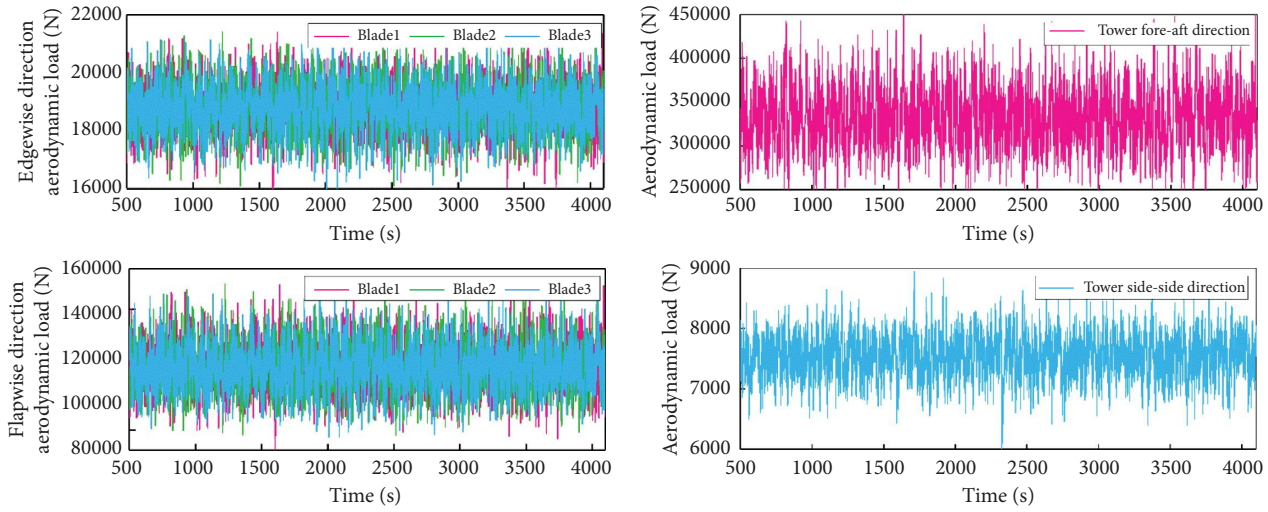

(a) (b)

Figure 7: Aerodynamic load: (a) blade and (b) tower.

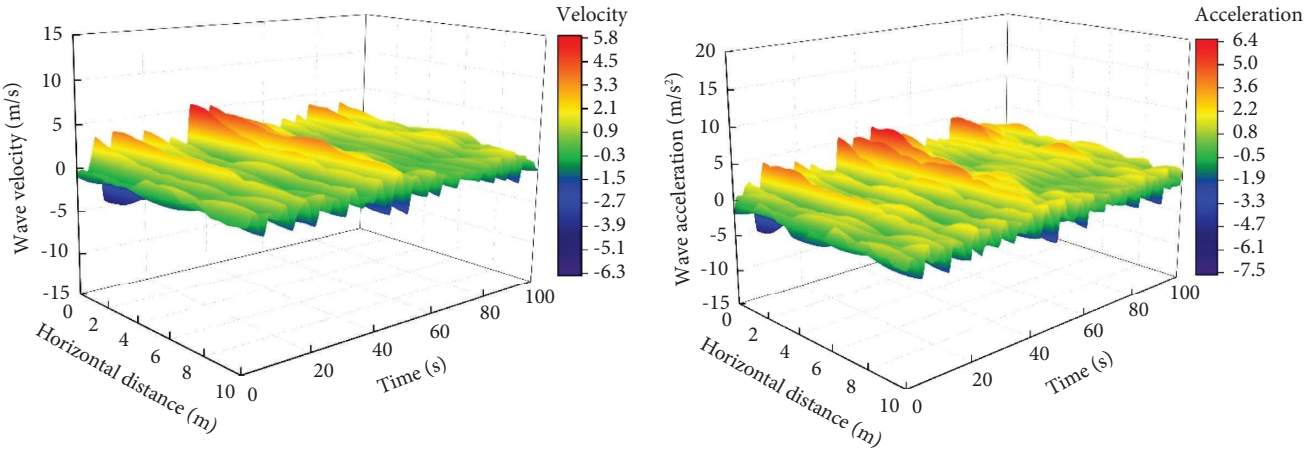

(a) (b)

Figure 8: (a) Wave velocity and (b) wave acceleration distributions in time and space.

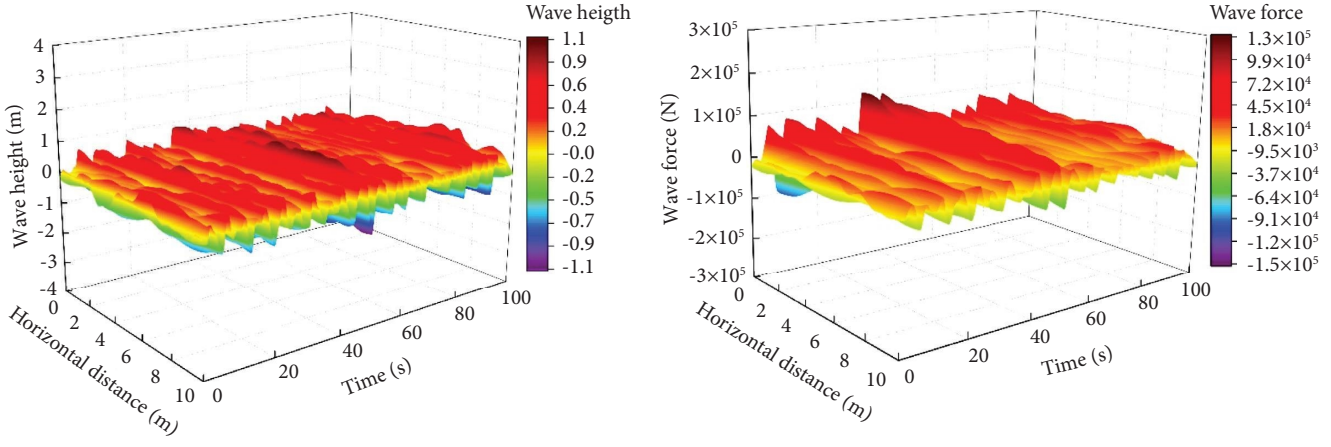

(a) (b)

Figure 9: (a) Wave height and (b) hydrodynamic load distributions in time and space.

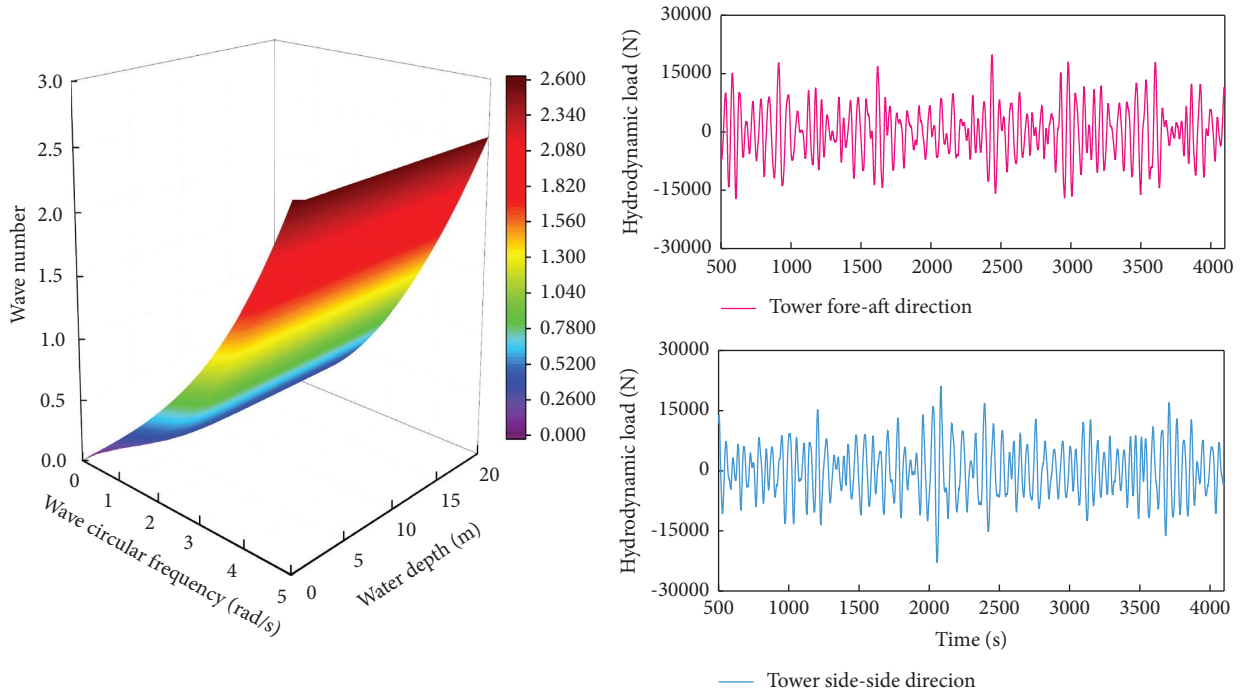

FIGURE 10: (a) Wave number and (b) hydrodynamic load.

parameters into equations (A1) to (A12) of Appendix A, the generalized mass and stiffness of the blade and tower for uncontrolled OWT and their fundamental frequencies are calculated as listed in Table 3.

As is shown in Table 3, the maximum frequency tolerance between OpenFAST and the developed model is only 2.244%, so this developed DOFs coupling model can reflect the structural characteristic and dynamic behavior in the dynamic analysis. Subsequently, the aerodynamic and hydrodynamic loads simulated by OpenFAST are replaced as the load vectors $\mathbf{Q_{wind}}$ $(\mathbf{t})$ and $\mathbf{Q_{wave}}$ $(\mathbf{t})$ to calculate the displacement responses at the tower top, respectively, and compared these responses of uncontrolled OWT with the calculation results of OpenFAST, as shown in Figure 11. When the servo-dynamic system is ignored, it can be found that the bidirectional displacement responses of the tower top from MATLAB calculation agree well with the OpenFAST simulation at the vast majority of time domain, so this developed DOFs coupling model can be effectively used to examine the vibration suppression competence of the 3D-PSTMD for OWT.

5.4. Devices Design

5.4.1. Dynamic Parameters of the OWT with 3D-PSTMD. The fundamental mode shapes of the blade in the in-plane and out-plane and the tower in the F-A or S-S directions are formulated [13] as

$$\begin{cases} \varphi_{bej}(\overline{r}) = -0.6952\overline{r}^6 + 2.3760\overline{r}^5 - 3.5772\overline{r}^4 + 2.5337\overline{r}^3 + 0.3627\overline{r}^2, \\ \varphi_{bfj}(\overline{r}) = -2.2555\overline{r}^6 + 4.7131\overline{r}^5 - 3.2452\overline{r}^4 + 1.7254\overline{r}^3 + 0.0622\overline{r}^2, \\ \varphi_t(\overline{h}) = -0.6952\overline{h}^6 + 2.3760\overline{h}^5 - 3.5772\overline{h}^4 + 2.5337\overline{h}^3 + 0.3627\overline{h}^2, \end{cases} \tag{45}$$

where shape functions of three blades corresponding to the fundamental vibration mode are the same, and $\overline{r} = r/61.5$ and $\overline{h} = h/87.6$ represent the normalized radial length of the blade and vertical height of the tower, respectively.

The soil and hydrodynamic effect is also modelled by linear springs and dashpots, as illustrated in Figure 3. The foundation translation stiffness coefficient k_{ft} is 1.03×10^{10} N/m, and the foundation rotational stiffness

Table 3: Fundamental frequencies of blade and tower.

Item		Blade		Tower	
		In-plane	Out-plane	F-A direction	S-S direction
Generalized mass (kg)		1.399×10^{3}	$9.09^{3}\times10^{2}$	4.120×10^{5}	4.133×10^{5}
Generalized stiffness (N/m)		6.560×10^{4}	1.650×10^{4}	1.724×10^{6}	1.658×10^{6}
Fundamental frequency (Hz)	OpenFAST	1.080	0.668	0.324	0.312
	MATLAB	1.090	0.678	0.326	0.319
Frequency tolerance (%)		0.926	1.497	0.617	2.244

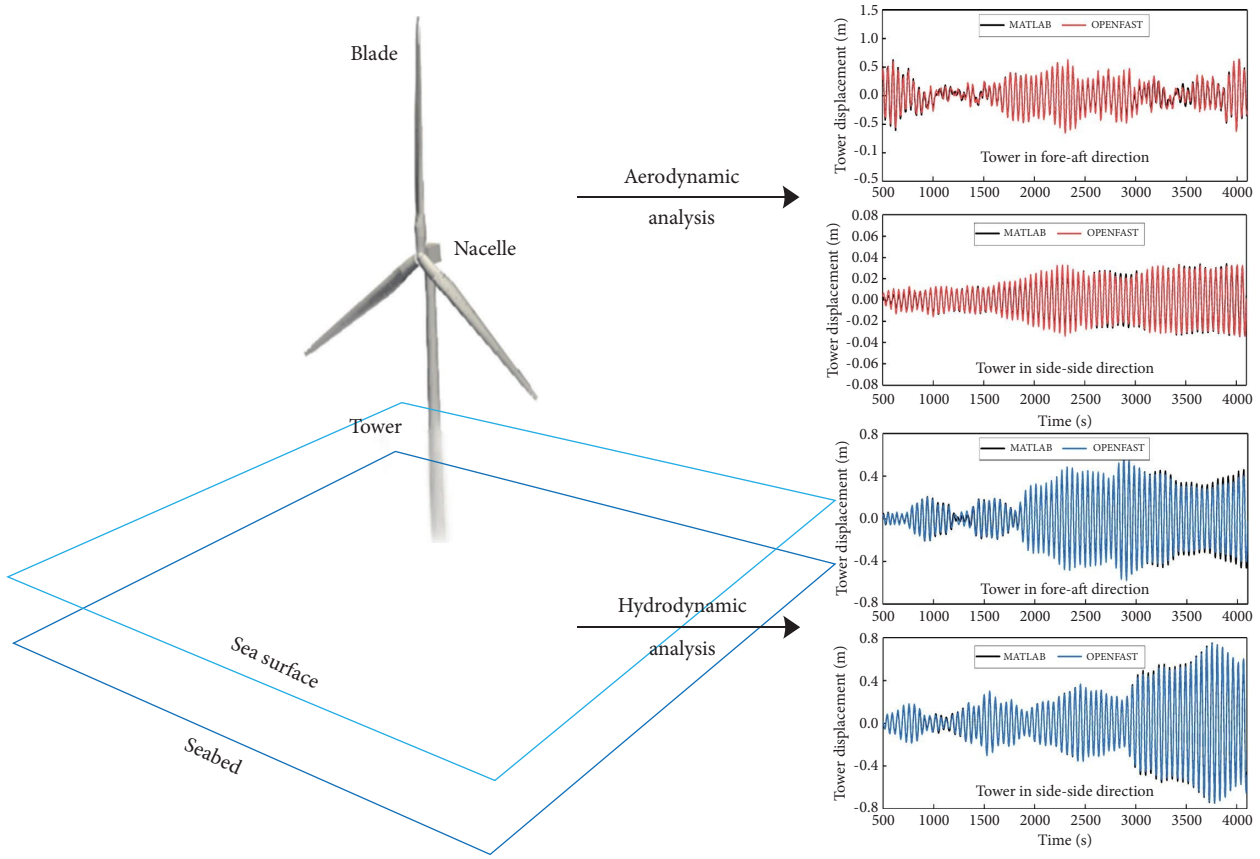

Figure 11: Response comparisons.

coefficients at F-A and S-S directions are assumed the same with k_{fr} equals 1.14×10^{12} N/m at F-A and S-S directions [29]. The foundation translation and rotational damping ratio are assumed the same with c_{ft} equals 0.6% to denote the clay soil condition.

5.4.2. Devices' Parameters. A traditional 3D pendulum TMD (3D-PTMD) is also studied for a comparison. The optimal frequency ratio and damping ratio of the 3D-PTMD can be obtained [13, 30] as

$$\begin{cases} L = \dfrac{g}{\left(4\pi^2 f_t^2 \mu_T^2\right)}, \\ \mu_T = 7.6\alpha_T^2 - 2.5\alpha_T + 1, \\ \zeta_T = -2.7\alpha_T^2 + \alpha_T + 0.062, \end{cases} \tag{46}$$

where L represents the physical pendulum length of the 3D-PTMD device, and f_t denotes the fundamental frequency of the OWT tower. α_T is the mass ratio between the

Table 4: Design parameters of 3D-PTMD and 3D-PSTMD.

Type	Mass (kg)	Pendulum length (m)	Prestressed tensile force (N)	Frequency ratio	Damping coefficient ((N/m/s))
3D-PTMD	3.48×10^3	7.2	0	0.98	6.17×10^2
3D-PSTMD	3.48×10^3	5.0	1.95×10^3	0.98	1.04×10^3

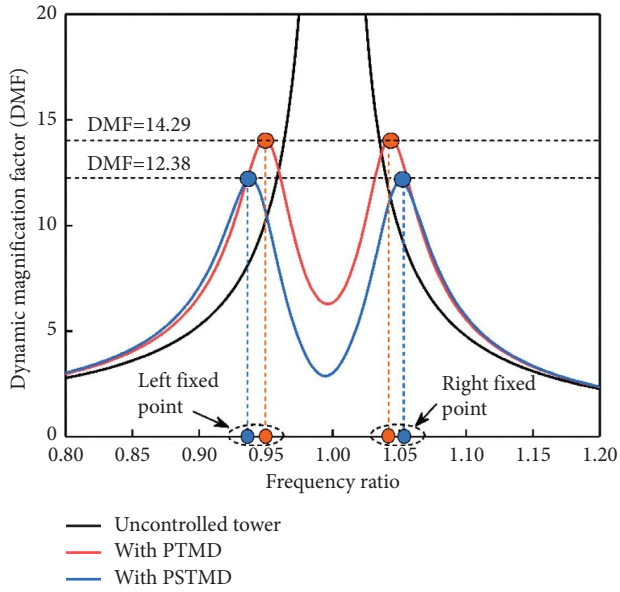

Figure 12: Frequency-response curves.

3D-PTMD and OWT. μ_T and ζ_T represent the optimal frequency ratio and damping ratio, respectively.

The cable tension of the 3D-PSTMD device can be described [17] as

$$f_P = \frac{(h_F - h_L)\left[2h_F M_P(k_t h_F + M_P g) - 2h_F M_O M_P g - 3(h_F - h_L)M_P^2 g\right]}{\left[2h_F^2 M_O + 3(h_F - h_L)^2 M_P - 2h_F(h_F - h_L)M_P\right]}, \tag{47}$$

where M_P and M_O denote the generalized mass of the 3D-PSTMD and OWT structure, respectively. k_t represents the lateral stiffness of the tower structure for the uncontrolled OWT, and its expression is listed in equation (A12) in Appendix A.

A single DOF (degree-of-freedom) wind turbine tower with a concentrated mass (representing the blades) is established, and the parameters' design method of the unidirectional PSTMD is derived in the studies in [17]. This paper developed a three-dimensional PS-TMD (3D-PSTMD) for vibration control of the OWT with the dynamic system modelled as coupling multiple DOFs of the blade, tower, and foundation. The tower member models from these two methods are same, and the PSTMD designs only depend on the dynamic parameters of the tower. This point can be also found in equations (B1) and (B7) of Appendixes A and B; only the DOFs q_7 and q_8 (representing the tower) are coupled with the PSTMD. Hence, to achieve the best tuning condition of the designed 3D-PSTMD, the optimal frequency ratio and damping ratio of the 3D-PSTMD can be taken as follows [17]:

$$\begin{cases} \mu_P = \sqrt{\dfrac{2-3\gamma_P}{2}}, \\ \zeta_P = \dfrac{\sqrt{2(2-3\gamma_P)\beta_P + \left(\gamma_P - \sqrt{\gamma_P^2 + (2-3\gamma_P)\beta_P}\right)^2}}{2\sqrt{4(1-\gamma_P) - 2\sqrt{\gamma_P^2 + (2-3\gamma_P)\beta_P}}}, \end{cases} \tag{48}$$

where μ_P and ζ_P represent the optimal frequency ratio and damping ratio of the 3D-PSTMD device, respectively. Symbols β_P and γ_P represent the tuning coefficients of the 3D-PSTMD device, which is described as

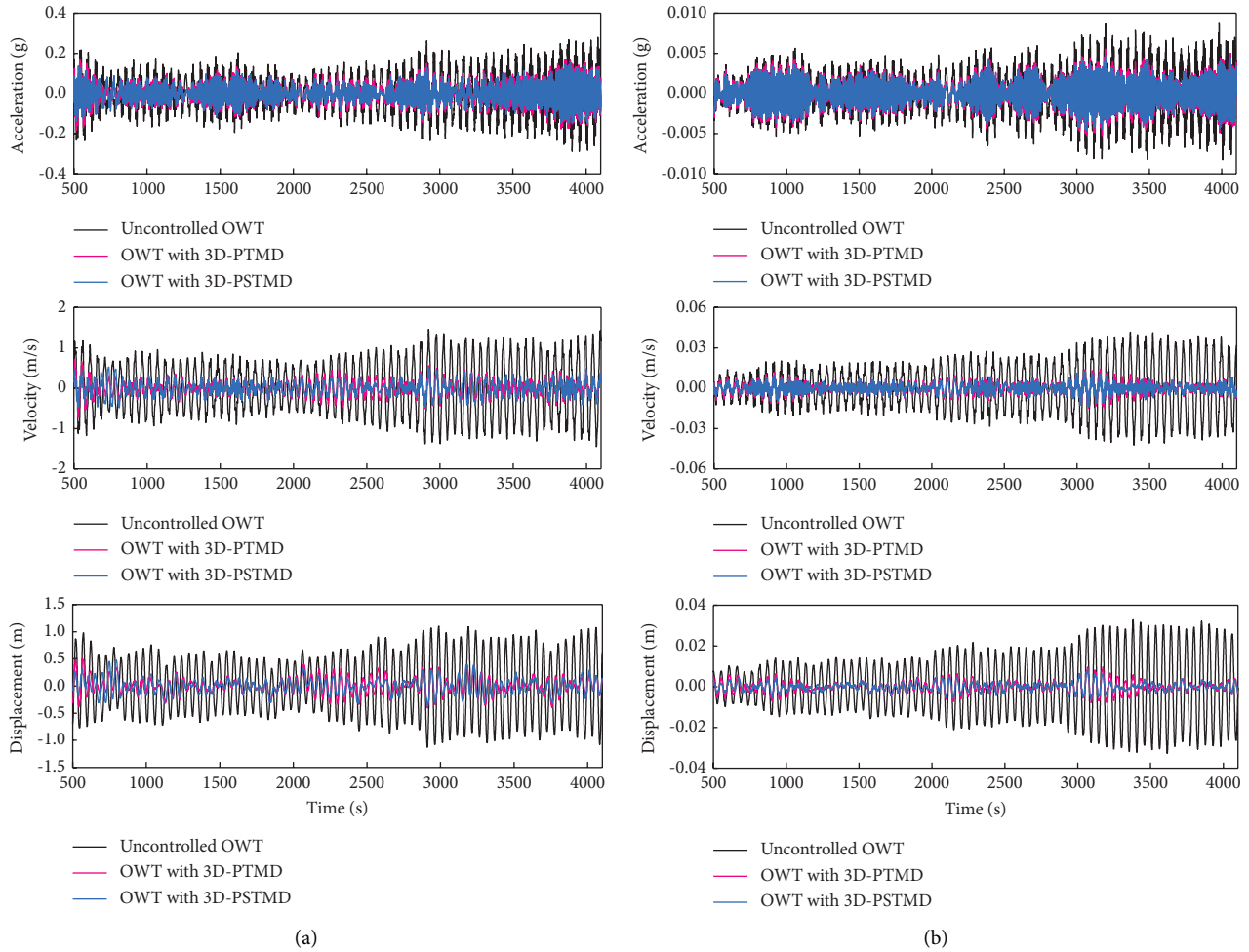

Figure 13: Dynamic responses of OWT tower under the aerodynamic load: (a) fore-aft direction and (b) side-side direction.

$$\begin{cases} \beta_P = \dfrac{(M_P g + f_P)^2 (h_F - h_L)}{(k_t h_L + M_P g + f_P)[(h_F - h_L) M_P g + h_L f_P]}, \\ \gamma_P = \dfrac{(M_P g + f_P)(h_F - h_L)}{h_F (k_t h_L + M_P g + f_P)}. \end{cases} \tag{49}$$

Since the mass ratio of the TMD device is generally 1%–3% of the primary structure [31], the mass ratios of 3D-PTMD and PS-TMD are set as 1% in this study. According to the OWT parameters mentioned above and equation (46), the pendulum length L of the 3D-PTMD is calculated as 7.2 m. The physical suspension height h_L of the 3D-PSTMD device is taken as 5 m for a better performance of the 3D-PSTMD. The design parameters of the 3D-PTMD and 3D-PSTMD with the same mass and frequency ratio can then be computed and are shown in Table 4.

In terms of the abovementioned design parameters, the frequency-response curves including uncontrolled OWT tower, OWT tower with 3D-PTMD, and 3D-PSTMD are plotted in Figure 12. Since these two dashpots are designed by using the optimal parameter design method from theoretical derivation [13, 17], their dynamic magnification factors (DMFs) between left and right fixed points are same. Meanwhile, the DMF of OWT tower with the 3D-PSTMD is smaller than the traditional 3D-PTMD; this is because the PSTMD well suppresses the dynamic displacement responses, and this point can be also found in Section 6.2.

6. Vibration Control Effect

6.1. Evaluation Indices R_1 and R_2. Two metrics are used to study quantitatively the vibration control performance, the maximal value index R_1, and the root mean square (RMS) index R_2, which may be described as follows:

$$\begin{cases} R_1 = \dfrac{\max|x_U| - \max|x_C|}{\max|x_U|}, \\ R_2 = \dfrac{\mathrm{rms}|x_U| - \mathrm{rms}|x_C|}{\mathrm{rms}|x_U|}, \end{cases} \tag{50}$$

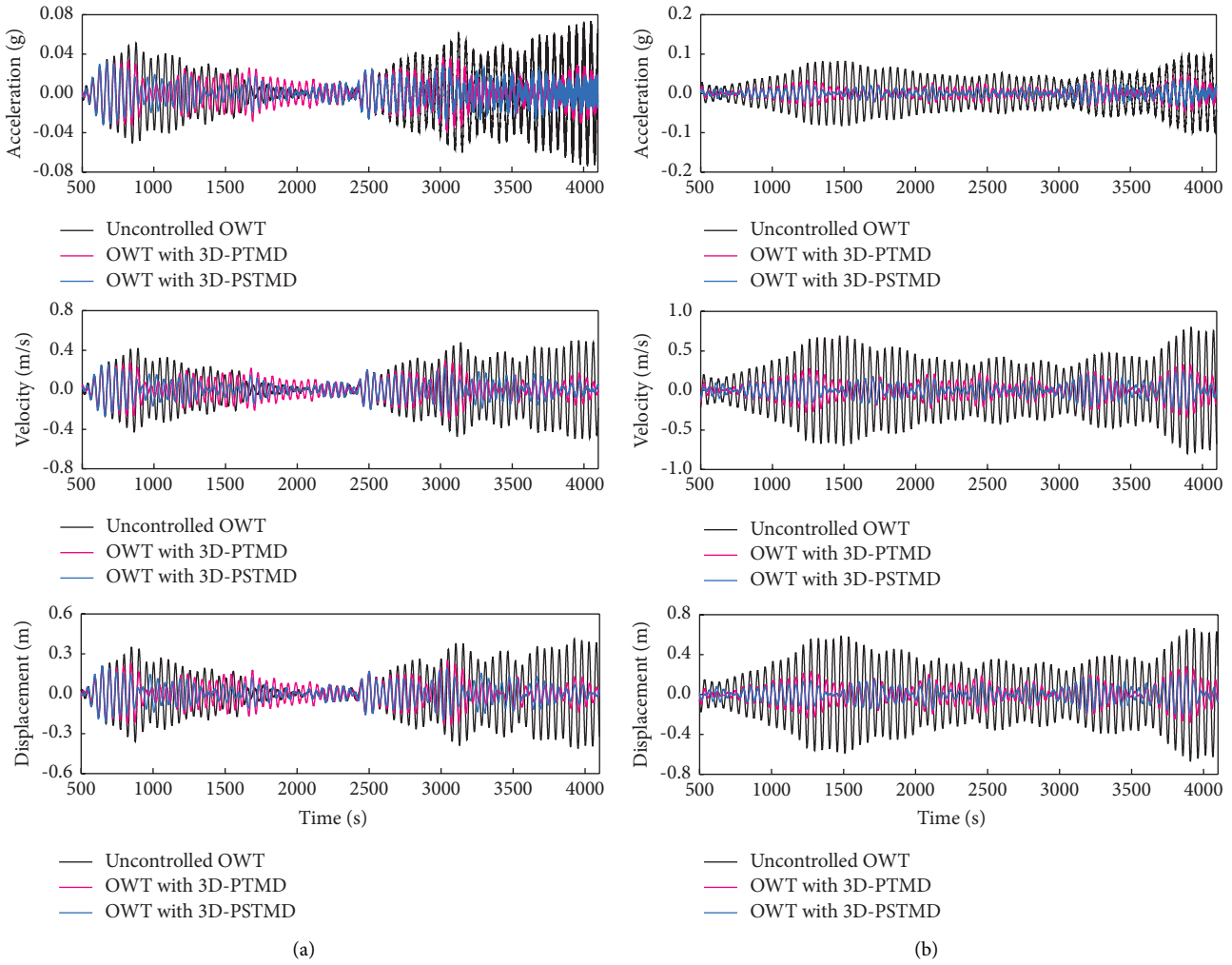

Figure 14: Dynamic responses of OWT tower under the hydrodynamic load: (a) fore-aft direction and (b) side-side direction.

where the symbol max represents the maximal value of the dynamic response, and the rms represents the corresponding RMS values. Subscripts C and U represent the dynamic responses with and without the 3D-PTMD or 3D-PSTMD, respectively.

6.2. Dynamic Time History Analysis. The dynamic responses are computed by using the Wilson-θ method in this paper. It is a numerical method with unconditional convergence, and the intermediate parameter θ is usually taken as 1.4 to ensure the unconditional convergence. With the OWT parameters obtained in Section 5.1, the corresponding matrices of equation (20) are calculated from Appendices A and B. Similar matrices of OWT coupled by the 3D-PTMD system are obtained from the studies in [23]. Considering the simulated aerodynamic and hydrodynamic loads in Section 5.2, the acceleration, velocity, and displacement responses at the top of the tower of the uncontrolled OWT, OWT controlled by 3D-PTMD and 3D-PSTMD are calculated, and they are plotted in Figures 13 and 14.

All the responses at the tower top of the OWT with the 3D-PTMD or 3D-PSTMD are obviously mitigated compared with the uncontrolled OWT structure when under the aerodynamic or hydrodynamic loads.

6.3. Performance Comparison. The effectiveness of vibration control performances of the 3D-PTMD and 3D-PSTMD is computed by using equation (50) when under the aerodynamic or hydrodynamic loads, as shown in Tables 5 and 6.

When under the aerodynamic force caused by wind loading, the 3D-PSTMD device outperforms the 3D-PTMD in reducing the peak acceleration response (F-A and S-S directions) with an improvement of approximately 9.7% and 11.0%, respectively. The index on the standard deviation of the acceleration response (F-A and S-S directions) can, respectively, be improved by approximately 7.0% and 6.8% by the 3D-PSTMD as compared to the 3D-PTMD. The proposed 3D-PSTMD can also improve the effectiveness of vibration mitigation on the peak-velocity response by 12.9% and 7.3% in fore-aft and side-side direction, respectively,

Table 5: Vibration control effectiveness when under aerodynamic load.

Devices	Direction	Acceleration (%)		Velocity (%)		Displacement (%)	
		R_1	R_2	R_1	R_2	R_1	R_2
3D-PTMD	Fore-aft	34.5	43.1	50.9	68.6	50.8	68.5
	Side-side	36.5	34.5	62.1	72.2	68.6	73.8
3D-PSTMD	Fore-aft	44.2	50.1	63.8	72.7	56.7	72.9
	Side-side	47.5	41.3	69.4	78.0	73.5	80.3

Table 6: Vibration control effectiveness when under hydrodynamic load.

Devices	Direction	Acceleration (%)		Velocity (%)		Displacement (%)	
		R_1	R_2	R_1	R_2	R_1	R_2
3D-PTMD	Fore-aft	50.2	45.2	41.1	46.2	40.7	46.6
	Side-side	55.1	65.0	59.3	65.1	57.7	64.5
3D-PSTMD	Fore-aft	56.3	53.1	49.5	54.7	49.3	55.0
	Side-side	68.3	73.5	70.5	73.9	70.0	73.4

relative to the 3D-PTMD. The index on the standard deviation of the velocity response is also increased by 4.1% and 5.8% relative to the 3D-PTMD in the fore-aft and side-side direction, respectively. The improvement in the effectiveness of vibration control of the peak-displacement response is 5.9% and 4.9% in the F-A and S-S directions, respectively, compared to the 3D-PTMD device. The index on the standard deviation of the displacement response is also increased by 4.4% and 6.5% in the fore-aft and side-side directions, respectively, compared to the 3D-PTMD.

When under the hydrodynamic force caused via the wave action, the 3D-PSTMD device outperforms the 3D-PTMD in reducing the peak acceleration response (F-A and S-S directions) with an improvement of approximately 6.1% and 13.2%, respectively. The index on the standard deviation of the acceleration response (F-A and S-S directions) can also be improved by around 7.9% and 8.5%, respectively, when compared to the 3D-PTMD. The proposed 3D-PSTMD can also promote the effectiveness of vibration control on the peak velocity response by 8.4% and 11.2% relative to the 3D-PTMD in F-A and S-S directions, respectively. The index on the standard deviation of the velocity response can also be increased by 8.5% and 8.8% in the F-A and S-S directions, respectively, relative to the 3D-PTMD device. Furthermore, the 3D-PSTMD can also enhance the vibration mitigation effectiveness of the peak displacement response by 8.6% and 12.3% in F-A and S-S directions, respectively, compared to the 3D-PTMD device. The index on the standard deviation of the displacement responses can also be enhanced by 8.4% and 8.9% in F-A and S-S directions, respectively, compared to the 3D-PTMD device.

7. Conclusions

The one-dimensional PSTMD developed by the authors for vibration mitigation of the offshore wind turbine tower (OWT) is extended to a 3D-PSTMD for vibration mitigation of a more realistic OWT system modelled as a multiple DOFs system with full coupling of the turbine blades, tower, and foundation. This enables separate consideration of the aerodynamic and hydrodynamic forces in the study of vibration mitigation at F-A and S-S directions. The dynamic model of multiple DOFs OWT system with the 3D-PSTMD is derived with the Lagrangian equation to explain the advantages of the 3D-PSTMD compared to the traditional tuned mass damper. The aerodynamic and hydrodynamic forces are generated via the BEM theory and Morrison equation, and the dynamic responses are computed by using the Wilson-θ method. The vibration mitigation capability of the 3D-PSTMD is evaluated in comparison to those from traditional three-dimensional pendulum TMD (3D-PTMD). The following major conclusions can be obtained as follows:

(1) Unlike the traditional 3D-PTMD, the 3D-PSTMD can provide additional lateral stiffness to the OWT which can slightly diminish the structural static displacement of OWT.

(2) Since the own frequency of the 3D-PSTMD device is synchronously tuned by changing cable tension and suspension height, the 3D-PSTMD system can be tuned with a larger modal damping coefficient than that from the traditional 3D-PTMD.

(3) Under the aerodynamic force caused by wind loading, the OWT with 3D-PSTMD performs better than the OWT with 3D-PTMD in the mitigation of the peak dynamic responses with over 5.9% and 4.9% improvements in the F-A and S-S directions, respectively. The standard deviation of dynamic responses (F-A and S-S directions) can also be improved by more than 4.1% and 5.8%, respectively, by the 3D-PSTMD when compared to those from the 3D-PTMD.

(4) Under the hydrodynamic force caused by the sea wave loading, the 3D-PSTMD outperforms the 3D-PTMD in reducing the peak dynamic responses (F-A and S-S directions) with an improvement of over 6.1% and 11.2%, respectively, compared to those from 3D-PTMD. The standard deviation of dynamic responses can also be improved by 7.9% and 8.5% in

the F-A and S-S directions, respectively, relative to the 3D-PTMD.

Appendix

A.

For the uncontrolled OWT structure, it is a coupled 12 DOFs dynamic system, and the corresponding mass matrix involved in equation (20) is expressed as follows:

$$\mathbf{M}=\begin{bmatrix} m_{11} & 0 & 0 & 0 & 0 & 0 & 0 & m_{18} & 0 & 0 & m_{111} & m_{112} \\ 0 & m_{22} & 0 & 0 & 0 & 0 & 0 & m_{28} & 0 & 0 & m_{211} & m_{212} \\ 0 & 0 & m_{33} & 0 & 0 & 0 & 0 & m_{38} & 0 & 0 & m_{311} & m_{312} \\ 0 & 0 & 0 & m_{44} & 0 & 0 & m_{47} & 0 & m_{49} & m_{410} & 0 & 0 \\ 0 & 0 & 0 & 0 & m_{55} & & m_{57} & 0 & m_{59} & m_{510} & 0 & 0 \\ 0 & 0 & 0 & 0 & 0 & m_{66} & m_{67} & 0 & m_{69} & m_{610} & 0 & 0 \\ 0 & 0 & 0 & 0 & 0 & 0 & m_{77} & 0 & m_{79} & m_{710} & 0 & 0 \\ m_{81} & m_{82} & m_{83} & 0 & 0 & 0 & 0 & m_{88} & 0 & 0 & m_{811} & m_{812} \\ 0 & 0 & 0 & m_{94} & m_{95} & m_{96} & m_{97} & 0 & m_{99} & m_{910} & 0 & 0 \\ 0 & 0 & 0 & m_{104} & m_{105} & m_{106} & m_{107} & 0 & m_{109} & m_{1010} & 0 & 0 \\ m_{111} & m_{112} & m_{113} & 0 & 0 & 0 & 0 & m_{118} & 0 & 0 & m_{1111} & m_{1112} \\ m_{121} & m_{122} & m_{123} & 0 & 0 & 0 & 0 & m_{128} & 0 & 0 & m_{1211} & m_{1212} \end{bmatrix}, \tag{A.1}$$

where m_{ij} is the influence coefficient of the mass matrix, which can be, respectively, described as

$$m_{jj}=\begin{cases} \int_0^R m_b(r)\varphi_{ej}^2(r)\mathrm{d}r, \quad j=1,2,3, \\ \int_0^R m_b(r)\varphi_{fj}^2(r)\mathrm{d}r, \quad j=4,5,6, \\ \left[3\int_0^R m_b(r)\mathrm{d}r+\int_0^H M_t(z)\varphi_t^2(z)\mathrm{d}z+M_n\right], \quad j=7,8, \\ \left[3\int_0^R m_b(r)\mathrm{d}r+\int_0^H M_t(z)\mathrm{d}z+M_n+M_{\mathrm{f}}\right], \quad j=9,11, \\ \left[3H^2\int_0^R m_b(r)\mathrm{d}r+3\int_0^H M_t(z)z^2\mathrm{d}z+H^2M_n+I_f\right], \quad j=10,12, \end{cases} \tag{A.2}$$

$$\begin{cases} m_{j8}=m_{8j}=m_{j11}=m_{11j}=\int_0^R m_b(r)\varphi_{ej}(r)\cos\theta_{bj}\mathrm{d}r, \quad j=1,2,3, \\ m_{j7}=m_{7j}=m_{j9}=m_{9j}=\int_0^R m_b(r)\varphi_{\mathrm{f}j}(r)\mathrm{d}r, \quad j=4,5,6, \end{cases} \tag{A.3}$$

$$\begin{cases} m_{j12}=m_{12j}=Hm_{j8}, \quad j=1,2,3, \\ m_{j10}=m_{10j}=Hm_{j7}, \quad j=4,5,6, \end{cases} \tag{A.4}$$

$$\begin{cases} m_{79} = m_{97} = m_{811} = m_{118} = \left[3\int_0^R m_b(r)\mathrm{d}r + \int_0^H M_t(z)\varphi_t(z)\mathrm{d}z + M_n\right], \\ m_{910} = m_{109} = m_{1112} = m_{1211} = \left[3H\int_0^R m_b(r)\mathrm{d}r + \int_0^H M_t(z)z\mathrm{d}z + HM_{\mathrm{n}}\right], \\ m_{710} = m_{107} = m_{812} = m_{128} = \left[3H\int_0^R m_b(r)\mathrm{d}r + \int_0^H M_t(z)\varphi_t(z)z\mathrm{d}z + HM_n\right]. \end{cases} \tag{A.5}$$

The damping matrix of the uncontrolled OWT system can be expressed as

$$\mathbf{C} = \begin{bmatrix} c_{11} & 0 & 0 & 0 & 0 & 0 & 0 & 0 & 0 & 0 & 0 & 0 \\ 0 & c_{22} & 0 & 0 & 0 & 0 & 0 & 0 & 0 & 0 & 0 & 0 \\ 0 & 0 & c_{33} & 0 & 0 & 0 & 0 & 0 & 0 & 0 & 0 & 0 \\ 0 & 0 & 0 & c_{44} & 0 & 0 & 0 & 0 & 0 & 0 & 0 & 0 \\ 0 & 0 & 0 & 0 & c_{55} & 0 & 0 & 0 & 0 & 0 & 0 & 0 \\ 0 & 0 & 0 & 0 & 0 & c_{66} & 0 & 0 & 0 & 0 & 0 & 0 \\ 0 & 0 & 0 & 0 & 0 & 0 & c_{77} & 0 & 0 & 0 & 0 & 0 \\ c_{81} & c_{82} & c_{83} & 0 & 0 & 0 & 0 & c_{88} & 0 & 0 & 0 & 0 \\ 0 & 0 & 0 & 0 & 0 & 0 & 0 & 0 & c_{99} & 0 & 0 & 0 \\ 0 & 0 & 0 & 0 & 0 & 0 & 0 & 0 & 0 & c_{1010} & 0 & 0 \\ c_{111} & c_{112} & c_{113} & 0 & 0 & 0 & 0 & 0 & 0 & 0 & c_{1111} & 0 \\ c_{121} & c_{122} & c_{123} & 0 & 0 & 0 & 0 & 0 & 0 & 0 & 0 & c_{1212} \end{bmatrix}, \tag{A.6}$$

where c_{ij} is the influence coefficient of the damping matrix, which are, respectively, described as

$$c_{jj} = \begin{cases} \alpha\int_0^R EI_{\mathrm{be}}(r)\varphi''_{\mathrm{be}j}(r)dr, & j = 1,2,3, \\ \alpha\int_0^R EI_{\mathrm{bf}}(r)\varphi''_{\mathrm{bf}j}(r)\mathrm{d}r, & j = 4,5,6, \\ \alpha\int_0^R EI_t(z)\varphi''_t(z)\mathrm{d}z, & j = 7, \\ \alpha\int_0^R EI_{\mathrm{t}}(z)\varphi''_t(z)\mathrm{d}z, & j = 8, \\ c_{\mathrm{ft}}, & j = 9, \\ c_{\mathrm{fr}}, & j = 10, \\ c_{\mathrm{ft}}, & j = 11, \\ c_{\mathrm{fr}}, & j = 12, \end{cases} \tag{A.7}$$

$$c_{8j} = c_{11j} = c_{12j} = -2\omega_b\int_0^R m_b(r)\varphi_{ej}(r)\sin\theta_{bj}\mathrm{d}r, \quad j = 1,2,3. \tag{A.8}$$

The stiffness matrix of the uncontrolled OWT system can be expressed as

$$\mathbf{K} = \begin{bmatrix} k_{11} & 0 & 0 & 0 & 0 & 0 & 0 & 0 & 0 & 0 & 0 & 0 \\ 0 & k_{22} & 0 & 0 & 0 & 0 & 0 & 0 & 0 & 0 & 0 & 0 \\ 0 & 0 & k_{33} & 0 & 0 & 0 & 0 & 0 & 0 & 0 & 0 & 0 \\ 0 & 0 & 0 & k_{44} & 0 & 0 & 0 & 0 & 0 & 0 & 0 & 0 \\ 0 & 0 & 0 & 0 & k_{55} & 0 & 0 & 0 & 0 & 0 & 0 & 0 \\ 0 & 0 & 0 & 0 & 0 & k_{66} & 0 & 0 & 0 & 0 & 0 & 0 \\ 0 & 0 & 0 & 0 & 0 & 0 & k_{77} & 0 & 0 & 0 & 0 & 0 \\ k_{81} & k_{82} & k_{83} & 0 & 0 & 0 & 0 & k_{88} & 0 & 0 & 0 & 0 \\ 0 & 0 & 0 & 0 & 0 & 0 & 0 & 0 & k_{99} & 0 & 0 & 0 \\ 0 & 0 & 0 & 0 & 0 & 0 & 0 & 0 & 0 & k_{1010} & 0 & 0 \\ k_{111} & k_{112} & k_{113} & 0 & 0 & 0 & 0 & 0 & 0 & 0 & k_{1111} & 0 \\ k_{121} & k_{122} & k_{123} & 0 & 0 & 0 & 0 & 0 & 0 & 0 & 0 & k_{1212} \end{bmatrix}, \tag{A.9}$$

where k_{ij} is the influence coefficient of the stiffness matrix, which is, respectively, described as

$$k_{jj} = \begin{cases} k_{be} + k_{gee} - k_{gre}\cos\theta_{bj} - \omega_b^2 m_{jj}, & j = 1, 2, 3, \\ k_{bf} + k_{gef} - k_{grf}\cos\theta_{bj}, & j = 4, 5, 6, \\ k_t, & j = 7, 8, \\ k_{ft}, & j = 9, \\ k_{fr}, & j = 10, \\ k_{ft}, & j = 11, \\ k_{fr}, & j = 12, \end{cases} \tag{A.10}$$

$$k_{8j} = k_{11j} = k_{12j} = -\omega_b^2 \int_0^R m_b(r)\varphi_{ej}(r)\cos\theta_{bj}\mathrm{d}r, \quad j = 1, 2, 3, \tag{A.11}$$

where k_t denotes the structural stiffness of the tower, and it is, respectively, obtained based on the structural generalized displacement theory [17] as

$$k_t = \int_0^H EI_t(z)\varphi''(z)^2\mathrm{d}z - M_n g\int_0^H \varphi'(z)^2\mathrm{d}z. \tag{A.12}$$

B.

The OWT coupled by the 3D-PSTMD system is a coupled 14 DOFs dynamic system, and its mass matrix in terms of equation (20) is described as

$$\mathbf{M}=\begin{bmatrix} m_{11} & 0 & 0 & 0 & 0 & 0 & 0 & m_{18} & 0 & 0 & m_{111} & m_{112} & 0 & 0 \\ 0 & m_{22} & 0 & 0 & 0 & 0 & 0 & m_{28} & 0 & 0 & m_{211} & m_{212} & 0 & 0 \\ 0 & 0 & m_{33} & 0 & 0 & 0 & 0 & m_{38} & 0 & 0 & m_{311} & m_{312} & 0 & 0 \\ 0 & 0 & 0 & m_{44} & 0 & 0 & m_{47} & 0 & m_{49} & m_{410} & 0 & 0 & 0 & 0 \\ 0 & 0 & 0 & 0 & m_{55} & 0 & m_{57} & 0 & m_{59} & m_{510} & 0 & 0 & 0 & 0 \\ 0 & 0 & 0 & 0 & 0 & m_{66} & m_{67} & 0 & m_{69} & m_{610} & 0 & 0 & 0 & 0 \\ 0 & 0 & 0 & m_{74} & m_{75} & m_{76} & m_{77} & 0 & m_{79} & m_{710} & 0 & 0 & m_{713} & 0 \\ m_{81} & m_{82} & m_{83} & 0 & 0 & 0 & 0 & m_{88} & 0 & 0 & m_{811} & m_{812} & 0 & m_{814} \\ 0 & 0 & 0 & m_{94} & m_{95} & m_{96} & m_{97} & 0 & m_{99} & m_{910} & 0 & 0 & m_{913} & 0 \\ 0 & 0 & 0 & m_{104} & m_{105} & m_{106} & m_{107} & 0 & m_{109} & m_{1010} & 0 & 0 & m_{1013} & 0 \\ m_{111} & m_{112} & m_{113} & 0 & 0 & 0 & 0 & m_{118} & 0 & 0 & m_{1111} & m_{1112} & 0 & m_{1114} \\ m_{121} & m_{122} & m_{123} & 0 & 0 & 0 & 0 & m_{128} & 0 & 0 & m_{1211} & m_{1212} & 0 & m_{1214} \\ 0 & 0 & 0 & 0 & 0 & 0 & m_{137} & 0 & m_{139} & m_{1310} & 0 & 0 & m_{1313} & 0 \\ 0 & 0 & 0 & 0 & 0 & 0 & 0 & m_{148} & 0 & 0 & m_{1411} & m_{1412} & 0 & m_{1414} \end{bmatrix}, \tag{B.1}$$

where the influence coefficients of the mass matrix for OWT coupled by the 3D-PSTMD system are formulated as equations (B2) and (B3), and the other influence coefficients of the mass matrix are consistent with equation (A1).

$$m_{jj}=\begin{cases} \left[3\int_0^R m_b(r)\mathrm{d}r+\int_0^H M(z)\varphi_{\mathrm{t}}^2(z)\mathrm{d}z+M_{\mathrm{n}}+M_{\mathrm{P}}\right], & j=7,8, \\ \left[3\int_0^R m_b(r)\mathrm{d}r+\int_0^H M(z)\mathrm{d}z+M_{\mathrm{n}}+M_{\mathrm{P}}+M_f\right], & j=9,11, \\ \left[3H^2\int_0^R m_b(r)\mathrm{d}r+3\int_0^H M(z)z^2\mathrm{d}z+H^2M_n+H^2M_P+I_f\right], & j=10,12, \\ M_P, & j=13,14, \end{cases} \tag{B.2}$$

$$\begin{cases} m_{79}=m_{97}=m_{811}=m_{118}=\left[3\int_0^R m_b(r)\mathrm{d}r+\int_0^H M(z)\varphi_{\mathrm{t}}(z)\mathrm{d}z+M_n+M_P\right], \\ m_{910}=m_{109}=m_{1112}=m_{1211}=\left[3H\int_0^R m_b(r)\mathrm{d}r+\int_0^H M(z)z\mathrm{d}z+HM_n+HM_P\right], \\ m_{710}=m_{107}=m_{812}=m_{128}=\left[3H\int_0^R m_b(r)\mathrm{d}r+\int_0^H M(z)\varphi_t(z)z\mathrm{d}z+HM_n+HM_P\right], \\ m_{713}=m_{137}=m_{913}=m_{139}=m_{814}=m_{148}=m_{1114}=m_{1411}=-M_P, \\ m_{1013}=m_{1310}=m_{1214}=m_{1412}=-HM_P. \end{cases} \tag{B.3}$$

The influence coefficients of the damping matrix for OWT coupled by the 3D-PSTMD system are described as

$$\mathbf{C}=\begin{bmatrix} c_{11} & 0 & 0 & 0 & 0 & 0 & 0 & 0 & 0 & 0 & 0 & 0 & 0 & 0 \\ 0 & c_{22} & 0 & 0 & 0 & 0 & 0 & 0 & 0 & 0 & 0 & 0 & 0 & 0 \\ 0 & 0 & c_{33} & 0 & 0 & 0 & 0 & 0 & 0 & 0 & 0 & 0 & 0 & 0 \\ 0 & 0 & 0 & c_{44} & 0 & 0 & 0 & 0 & 0 & 0 & 0 & 0 & 0 & 0 \\ 0 & 0 & 0 & 0 & c_{55} & 0 & 0 & 0 & 0 & 0 & 0 & 0 & 0 & 0 \\ 0 & 0 & 0 & 0 & 0 & c_{66} & 0 & 0 & 0 & 0 & 0 & 0 & 0 & 0 \\ 0 & 0 & 0 & 0 & 0 & 0 & c_{77} & 0 & 0 & 0 & 0 & 0 & c_{713} & 0 \\ c_{81} & c_{82} & c_{83} & 0 & 0 & 0 & 0 & c_{88} & 0 & 0 & 0 & 0 & 0 & c_{814} \\ 0 & 0 & 0 & 0 & 0 & 0 & 0 & 0 & c_{99} & 0 & 0 & 0 & 0 & 0 \\ 0 & 0 & 0 & 0 & 0 & 0 & 0 & 0 & 0 & c_{1010} & 0 & 0 & 0 & 0 \\ c_{111} & c_{112} & c_{113} & 0 & 0 & 0 & 0 & 0 & 0 & 0 & c_{1111} & 0 & 0 & 0 \\ c_{121} & c_{122} & c_{123} & 0 & 0 & 0 & 0 & 0 & 0 & 0 & 0 & c_{1212} & 0 & 0 \\ 0 & 0 & 0 & 0 & 0 & 0 & c_{137} & 0 & 0 & 0 & 0 & 0 & c_{1313} & 0 \\ 0 & 0 & 0 & 0 & 0 & 0 & 0 & c_{148} & 0 & 0 & 0 & 0 & 0 & c_{1414} \end{bmatrix}, \tag{B.4}$$

where the influence coefficients of the damping matrix for OWT coupled by the 3D-PSTMD can be formulated as equations (B5) and (B6), and the other influence coefficients of the damping matrix are consistent with equation (A6).

$$c_{jj}=\begin{cases} \alpha\int_0^R EI_t(z)\varphi_t''(z)\mathrm{d}z+\varphi_{tP}^2 c_{Pf}, & j=7, \\ \alpha\int_0^R EI_t(z)\varphi_t''(z)\mathrm{d}z+\varphi_{\mathrm{tP}}^2 c_{\mathrm{Ps}}, & j=8, \\ c_{\mathrm{Pf}}, & j=13, \\ c_{\mathrm{Ps}}, & j=14, \end{cases} \tag{B.5}$$

$$\begin{cases} c_{713}=c_{137}=-\varphi_{tP}c_{\mathrm{P}x}, \\ c_{814}=c_{148}=-\varphi_{tP}c_{Py}. \end{cases} \tag{B.6}$$

The stiffness matrix of OWT coupled by the 3D-PSTMD device is formulated as

$$\mathbf{K}=\begin{bmatrix} k_{11} & 0 & 0 & 0 & 0 & 0 & 0 & 0 & 0 & 0 & 0 & 0 & 0 & 0 \\ 0 & k_{22} & 0 & 0 & 0 & 0 & 0 & 0 & 0 & 0 & 0 & 0 & 0 & 0 \\ 0 & 0 & k_{33} & 0 & 0 & 0 & 0 & 0 & 0 & 0 & 0 & 0 & 0 & 0 \\ 0 & 0 & 0 & k_{44} & 0 & 0 & 0 & 0 & 0 & 0 & 0 & 0 & 0 & 0 \\ 0 & 0 & 0 & 0 & k_{55} & 0 & 0 & 0 & 0 & 0 & 0 & 0 & 0 & 0 \\ 0 & 0 & 0 & 0 & 0 & k_{66} & 0 & 0 & 0 & 0 & 0 & 0 & 0 & 0 \\ 0 & 0 & 0 & 0 & 0 & 0 & k_{77} & 0 & 0 & 0 & 0 & 0 & k_{713} & 0 \\ k_{81} & k_{82} & k_{83} & 0 & 0 & 0 & 0 & k_{88} & 0 & 0 & 0 & 0 & 0 & k_{814} \\ 0 & 0 & 0 & 0 & 0 & 0 & 0 & 0 & k_{99} & 0 & 0 & 0 & 0 & 0 \\ 0 & 0 & 0 & 0 & 0 & 0 & 0 & 0 & 0 & k_{1010} & 0 & 0 & 0 & 0 \\ k_{111} & k_{112} & k_{113} & 0 & 0 & 0 & 0 & 0 & 0 & 0 & k_{1111} & 0 & 0 & 0 \\ k_{121} & k_{122} & k_{123} & 0 & 0 & 0 & 0 & 0 & 0 & 0 & 0 & k_{1212} & 0 & 0 \\ 0 & 0 & 0 & 0 & 0 & 0 & k_{137} & 0 & 0 & 0 & 0 & 0 & k_{1313} & 0 \\ 0 & 0 & 0 & 0 & 0 & 0 & 0 & k_{148} & 0 & 0 & 0 & 0 & 0 & k_{1414} \end{bmatrix}, \tag{B.7}$$

where the influence coefficients of the stiffness matrix for OWT coupled by the 3D-PSTMD system are formulated as equations (B8) and (B9), and the other influence coefficients of the damping matrix are consistent with equation (A9).

$$k_{jj} = \begin{cases} \int_0^H EI_t(z)\varphi''(z)^2 \mathrm{d}z - M_n g \int_0^H \varphi'(z)^2 \mathrm{d}z + \dfrac{f_{\mathrm{P}}\left(\varphi_{\mathrm{tP}}^2 - \varphi_{\mathrm{tF}}^2\right)}{h_F - h_L}, & j = 7, 8, \\ \dfrac{M_P g + f_P}{h_L} + \dfrac{f_P}{h_F - h_L}, & j = 13, 14, \end{cases} \tag{B.8}$$

$$k_{713} = k_{137} = k_{814} = k_{148} = -\frac{f_P\left(\varphi_{\mathrm{tP}} - \varphi_{\mathrm{tF}}\right)}{h_F - h_L}. \tag{B.9}$$

Data Availability

The data used to support the findings of this study are available from the corresponding author upon reasonable request.

Conflicts of Interest

The authors declare that there are no conflicts of interest regarding the publication of this paper.

Acknowledgments

This project was funded through the National Natural Science Foundation of China (52221002 and 52078084), the National Natural Science Foundation of Chongqing (cstc2021jcyj-msxmX0623), and the 111 project of the Ministry of Education and the Bureau of Foreign Experts of China (grant no. B18062).

References

[1] H. R. Zuo, J. Zhang, G. K. Yuan, and S. Y. Zhu, "Wind- and sea wave-induced response mitigations of offshore wind turbines using track nonlinear energy sinks," *Structural Control and Health Monitoring*, vol. 29, no. 9, 2022.

[2] C. Sun, V. Jahangiri, and H. Sun, "Adaptive bidirectional dynamic response control of offshore wind turbines with time-varying structural properties," *Structural Control and Health Monitoring*, vol. 28, no. 11, 2021.

[3] Q. L. Cai and S. Y. Zhu, "The nexus between vibration-based energy harvesting and structural vibration control: a comprehensive review," *Renewable and Sustainable Energy Reviews*, vol. 155, Article ID 111920, 2022.

[4] B. Fitzgerald and B. Basu, "Vibration control of wind turbines: recent advances and emerging trends," *International Journal of Sustainable Materials and Structural Systems*, vol. 4, no. 2/3/4, p. 347, 2020.

[5] H. R. Zuo, K. M. Bi, and H. Hao, "A state-of-the-art review on the vibration mitigation of wind turbines," *Renewable and Sustainable Energy Reviews*, vol. 121, Article ID 109710, 2020.

[6] D. Chen, S. S. Huang, C. G. Huang, and R. W. Liu, "Passive control of jacket–type offshore wind turbine vibrations by single and multiple tuned mass dampers," *Marine Structures*, vol. 77, Article ID 102938, 2021.

[7] H. M. Liu, S. X. Yang, W. Tian, M. Zhao, X. L. Yuan, and B. F. Xu, "Vibration reduction strategy for offshore wind turbines," *Applied Sciences*, vol. 10, no. 17, p. 6091, 2020.

[8] D. C. Nguyen, "Optimal parameters of tuned mass dampers for an inverted pendulum with two degrees of freedom," *Proceedings of the Institution of Mechanical Engineers- Part K: Journal of Multi-body Dynamics*, vol. 235, no. 2, pp. 281–293, 2021.

[9] G. B. Colherinhas, M. V. G. de Morais, M. A. M. Shzu, and S. M. Avila, "Optimal pendulum tuned mass damper design applied to high towers using genetic algorithms: two-DOF modeling," *International Journal of Structural Stability and Dynamics*, vol. 19, no. 10, Article ID 1950125, 2019.

[10] M. Verma, M. K. Nartu, and A. Subbulakshmi, "Optimal TMD design for floating offshore wind turbines considering model uncertainties and physical constraints," *Ocean Engineering*, vol. 243, Article ID 110236, 2022.

[11] L. Valentina, A. Gioacchino, F. Giuseppe, R. Carlo, and A. Felice, "A two-degree-of-freedom tuned mass damper for offshore wind turbines on floating spar supports," *Marine Structures*, vol. 23, 2022.

[12] V. Jahangiri, C. Sun, and F. Kong, "Study on a 3D pounding pendulum TMD for mitigating bi-directional vibration of offshore wind turbines," *Engineering Structures*, vol. 241, Article ID 112383, 2021.

[13] C. Sun and V. Jahangiri, "Bi-directional vibration control of offshore wind turbines using a 3D pendulum tuned mass damper," *Mechanical Systems and Signal Processing*, vol. 105, pp. 338–360, 2018.

[14] K. A. Shah, F. T. Meng, Y. Li et al., "A synthesis of feasible control methods for floating offshore wind turbine system dynamics," *Renewable and Sustainable Energy Reviews*, vol. 152, 2021.

[15] J. López-Queija, E. Robles, J. Jugo, and S. Alonso-Quesada, "Review of control technologies for floating offshore wind turbines," *Renewable and Sustainable Energy Reviews*, vol. 167, Article ID 112787, 2022.

[16] S. Chapain and A. M. Aly, "Vibration attenuation in wind turbines: a proposed robust pendulum pounding TMD," *Engineering Structures*, vol. 233, Article ID 111891, 2021.

[17] G. Liu, Z. B. Lei, and H. Wang, "Investigation and optimization of a pre-stressed tuned mass damper for wind turbine tower," *Structural Control and Health Monitoring*, vol. 29, no. 3, 2021.

[18] M. Popescu, P. Popescu, and H. Ramos, "Some new discretizations of the Euler–Lagrange equation," *Communications*

in Nonlinear Science and Numerical Simulation, vol. 103, Article ID 106002, 2021.

[19] A. Kareem, L. Hu, Y. L. Guo, and D. K. Kwon, "Generalized wind loading chain: time-frequency modeling framework for nonstationary wind effects on structures," *Journal of Structural Engineering*, vol. 145, no. 10, 2019.

[20] A. Kareem and Y. Zhou, "Gust loading factor—past, present and future," *Journal of Wind Engineering and Industrial Aerodynamics*, vol. 91, no. 12-15, pp. 1301–1328, 2003.

[21] Y. Kim, H. A. Madsen, M. Aparicio-Sanchez, G. Pirrung, and T. Lutz, "Assessment of blade element momentum codes under varying turbulence levels by comparing with blade resolved computational fluid dynamics," *Renewable Energy*, vol. 160, pp. 788–802, 2020.

[22] O. L. Hansen Martin, *Aerodynamics of Wind Turbines*, Taylor and Francis, Oxfordshire, UK, 2015.

[23] G. Y. Xin, H. Deng, and G. L. Zhong, "Closed-form dynamics of a 3-DOF spatial parallel manipulator by combining the Lagrangian formulation with the virtual work principle," *Nonlinear Dynamics*, vol. 86, no. 2, pp. 1329–1347, 2016.

[24] C. Jin, "Comparison of potential theory and morison equation for deformable horizontal cylinders," *Sustainable Marine Structures*, vol. 4, no. 2, pp. 1–10, 2022.

[25] Y. Wan, R. Z. Qu, Y. S. Dai, and X. Y. Zhang, "Research on the applicability of the E spectrum and PM spectrum as the first guess spectrum of SAR wave spectrum inversion," *IEEE Access*, vol. 8, pp. 169082–169095, 2020.

[26] S. M. Jung, S. R. Kim, A. Patil, and L. C. Hung, "Effect of monopile foundation modeling on the structural response of a 5-MW offshore wind turbine tower," *Ocean Engineering*, vol. 109, pp. 479–488, 2015.

[27] H. Meng, D. Y. Jin, L. Li, and Y. Q. Liu, "Analytical and numerical study on centrifugal stiffening effect for large rotating wind turbine blade based on NREL 5 MW and WindPACT 1.5 MW models," *Renewable Energy*, vol. 183, pp. 321–329, 2022.

[28] J. Jonkman, S. Butterfield, W. Musial, and G. Scott, "Definition of a 5-mw reference wind turbine for offshore system development," National Renewable Energy Laboratory, Colorado, CO, USA, NREL/TP-500-38060, 2009.

[29] W. Carswell, J. Johansson, F. Løvholt et al., "Foundation damping and the dynamics of offshore wind turbine monopiles," *Renewable Energy*, vol. 80, pp. 724–736, 2015.

[30] R. R. Gerges and B. J. Vickery, "Optimum design of pendulum-type tuned mass dampers," *The Structural Design of Tall and Special Buildings*, vol. 14, no. 4, pp. 353–368, 2005.

[31] M. M. Americano da Costa, D. A. Castello, C. Magluta, and N. Roitman, "On the optimal design and robustness of spatially distributed tuned mass dampers," *Mechanical Systems and Signal Processing*, vol. 150, Article ID 107289, 2021.